Longitudinal dependence of ionospheric irregularities to maximum ring current and PPEF sensed by GNSS and magnetometers during the storm of 4 November 2021

Nadia Imtiaz[1], Teshome Dugassa Feyissa[2], Andres Calabia[3], and Anton Kashcheyev[4]

[1]Theoretical Physics Divison
[2]Space Science and Geospatial Institute
[3]School of Remote Sensing & Geomatic Engineering, Nanjing University of Information Science and Technology
[4]University of New Brunswick

May 2, 2023

Abstract

We employ multi-instrumental data to investigate the behavior of equatorial and low latitude ionosphere during the geomagnetic storm of November 3-6, 2021. We used TEC data obtained from GPS receiver stations located in the equatorial and low-latitudes of the Asian, African, and American sectors. It is found that the storm-time ionization level varies significantly in the trough and crest of EIA region over the three longitudes. ROTI is used to estimate the occurrence of ionospheric plasma irregularities during the storm. Usually, the main phase of the geomagnetic storm triggers the equatorial plasma irregularities and the recovery phase suppresses the occurrence of them. Here, we observed inhibition of the plasma irregularities over the three sectors during the main phase of the storm. We suspect this may be due to the injection of the PEFs which occur between local midnight and around noon during the main phase. The PEFs restrict the diffusion of plasma and therefore, suppress the occurrence of plasma irregularities during the main phase. During the recovery phase, moderate ionospheric irregularities occurred at local midnight in the American sector. In the African sector, the occurrence of weak irregularities can be seen before midnight on November 5 and 6. However, the Asian sector does not exhibit noticeable ionospheric irregularities during the storm. We conclude that the longitudinal variation in the development of ionospheric irregularities can be influenced by factors such as local time occurrence of maximum ring current, PPEF, disturbance wind dynamo electric field, and shielding electric field.

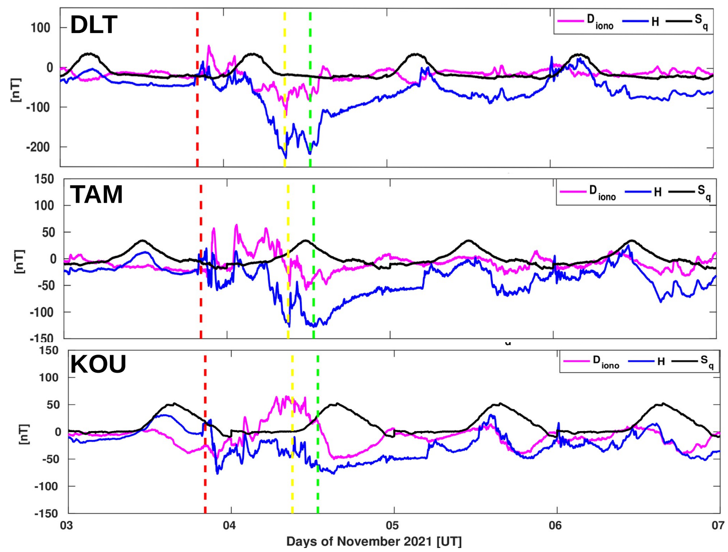

DLT
TAM
KOU
D_{iono}
H
S_q
[nT]
Days of November 2021 [UT]

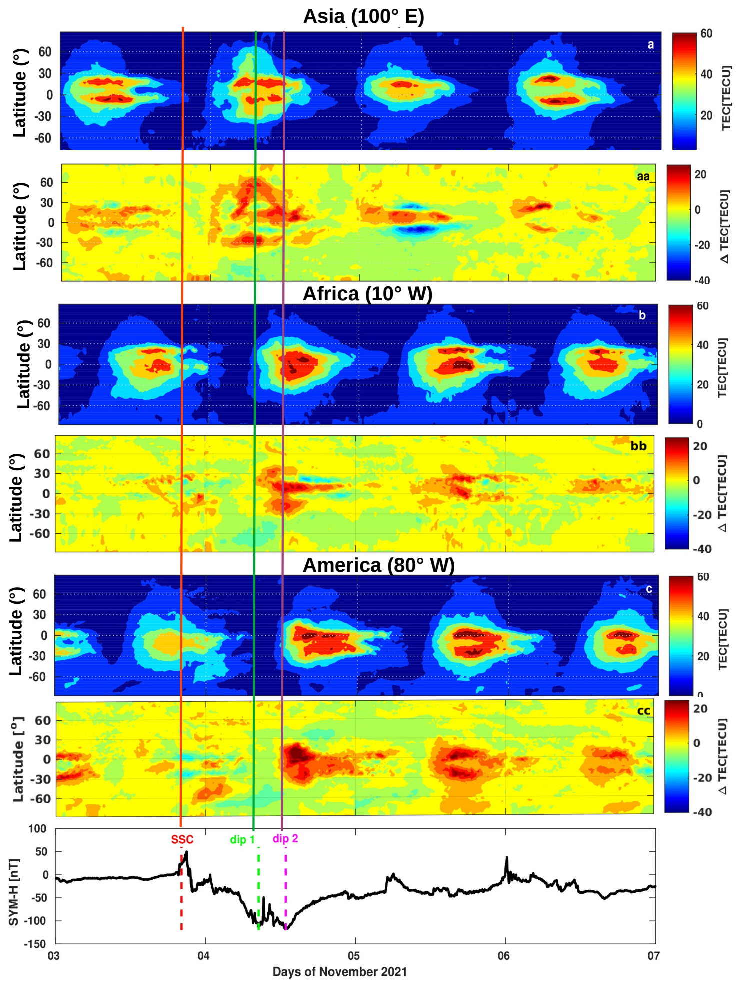
Asia (100° E)
Africa (10° W)
America (80° W)
Latitude (°)
TEC[TECU]
Δ TEC[TECU]
SSC
dip 1
dip 2
SYM-H [nT]
Days of November 2021

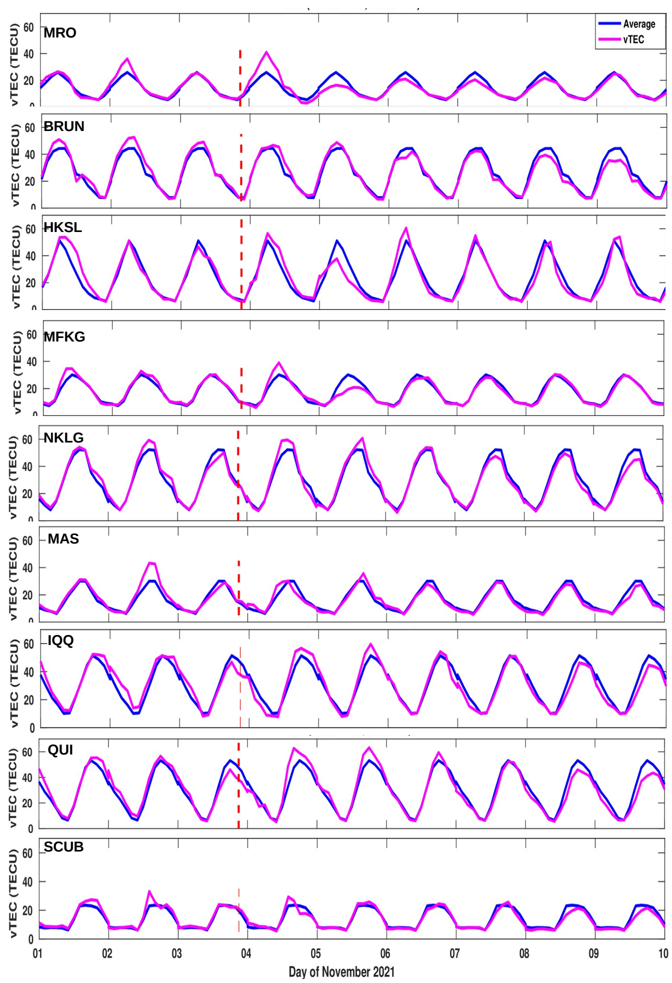
MRO
BRUN
HKSL
MFKG
NKLG
MAS
IQQ
QUI
SCUB
Average
vTEC
vTEC (TECU)
Day of November 2021
01
02
03
04
05
06
07
08
09
10

Longitudinal dependence of ionospheric irregularities to maximum ring current and PPEF sensed by GNSS and magnetometers during the storm of 4 November 2021

Nadia Imtiaz[1], Teshome Duggasa[2], Andres Calabia[3], and Anton Kashcheyev[4]

[1]Theoretical Physics Division, PINSTECH, Islamabad, Pakistan
[2]Space Science Geospatial Institute, Entoto Observatory and Research Center, Addis Ababa, Ethiopia
[3]Department of Physics and Mathematics, University of Acala, 28801-Alcalá de Henares (Madrid), Spain.
[4]Department of Physics, University of New Brunswick, Canada

Key Points:

- Ionospheric Irregularities
- Geomagnetic Storms
- Penetration Electric Field
- Wavelet Power Spectrum

Corresponding author: Nadia Imtiaz, `nhussain@ualberta.ca`

Abstract

In this study, we employ multi-instrumental data to investigate the behavior of equatorial and low latitude ionosphere during the geomagnetic storm of November 3-6, 2021. We used Total Electron Content (TEC) data obtained from Global Positioning System (GPS) receiver stations located in the equatorial and low-latitudes of the Asian, African, and American sectors. It is found that the storm-time ionization level varies significantly in the trough and crest of the equatorial ionization anomaly (EIA) region over the three longitudes. The rate of TEC change index (ROTI) shows the ionospheric plasma bubble irregularities during the storm. Strong ionospheric irregularities were observed over the American sector, prior to the storm showing the impact of the High-Speed Solar Wind Stream (HSSWS). Usually, the main phase of the geomagnetic storm triggers the equatorial plasma bubble irregularities and the recovery phase suppresses the occurrence of these irregularities. However, in this study, we observed inhibition of the plasma irregularities over the three sectors during the main phase of the storm. We suspect this may be due to the injection of the Penetration Electric Fields (PEFs) which occur between local midnight and around noon during the main phase. The PEFs restrict the diffusion of plasma and therefore, suppress the occurrence of plasma irregularities during the main phase. During the recovery phase, moderate ionospheric irregularities occurred at local midnight in the American sector on November 5 and 6. In the African sector, the occurrence of weak irregularities can be seen before midnight on November 5 and 6. However, the Asian sector does not exhibit noticeable ionospheric irregularities during the storm. The longitudinal variation in the generation of plasma irregularities can be associated with the local time at maximum negative excursion of the SYM-H index and the electric field. We conclude that the development of ionospheric irregularities can be influenced by factors such as local time occurrence of maximum ring current, prompt PEF, disturbance wind dynamo electric field, and shielding electric field.

1 Introduction

Highly dynamical conditions of the terrestrial atmosphere, ionosphere, magnetosphere, and interplanetary space can cause malfunctioning/non-operational situations in the technological/biological systems (A K Singh, 2021). The mitigation of these adverse effects needs in depth understanding of space weather phenomena by using both physics-based and empirical relations (M J Owens, 2021). Higher frequency of occurrence of geomagnetic storms at solar maximum than at solar minimum has been proven in the literature (Dalton, 1834; Sabine, 1852; Feynman & Crooker, 1978). This empirical trend can be applicable to moderate space weather events. For extreme space weather events, however, it is difficult to statistically establish patterns of occurrence. Therefore, the debate is whether the occurrence probability of extreme space weather events can be related to the 11 years solar cycle. In this context, (M J Owens, 2021) tested 150-year data of global geomagnetic activity with a number of probabilistic models to demonstrate the dependency of extreme events on the solar cycle. It was found that storms of all magnitudes are more frequent during an active phase (solar maximum) than during a quiet phase (solar minimum). Moreover, it was reported that extreme events are more frequent during larger magnitude solar cycles. Also, extreme events usually occur earlier in even cycles and later in odd cycles.

Energetic space weather events such as Coronal Mass Ejections (CMEs) and Corotating Interaction Regions (CIRs) are the main drivers of geomagnetic storms and can cause energy transfer from the solar wind into the magnetosphere (Lakhina & Tsurutani, 2016). CMEs travel from the solar corona to the interplanetary space, commonly characterized by a strong rotating magnetic field, a small ratio between plasma pressure and magnetic pressure, a low ion temperature, a high proton density, and by a high speed (J T Gosling, 1991; M Neugebauer, 1997; Gopalswamy, 2006). CME-driven geomagnetic storms are generally intense and their occurrence is connected to sunspot dynamics. These storms have short-duration recovery phase (1 or 2 days) and are commonly observed during high solar activity (A Balogh, 1999; Gopalswamy, 2004; B T Tsurutani, 1995). The energy input into the magnetosphere-ionosphere-thermosphere (MIT) system is mainly controlled by the Interplanetary Magnetic Field (IMF) and by the solar wind conditions. During prolonged periods of southward IMF B_z ($B_z < 0$), the dayside magnetic re-connection leads to the deposition of energy into the MIT system. This energy is converted into Joule heating and it modifies the thermospheric circulation and the distribution of neutral temperature, density and composition (T J Fuller-Rowell, 1994; Richmond & Matsushita, 1975; W D Gonzalez, 1994; Y Kamide, 1998; G Prolss, 1991).

The magnitude and occurrence of positive/negative ionospheric disturbances due to geomagnetic storms depend on latitude, local time, and other factors, including solar variability (Buonsanto, 1999; N M Pedatella, 2009; A Calabia, 2021). The storm induced ionospheric disturbances are due to the effect of the prompt penetration electric fields (PPEFs) and disturbance dynamo electric fields (DDEFs) (Blanc & Richmond, 1980). During southward turning of IMF Bz, the interplanetary electric field mapped to high latitudes as dawn-dusk electric field which penetrates into equatorial and low-latitude ionosphere, known as PPEFs or under shielding electric field. The polarity of PPEF is eastward (westward) on the dayside (nightside). During northward IMF Bz, the over-shielding electric field penetrates to the low-latitudes with polarity westward (eastward) on the dayside (nightside). Regardless of its orientation, the PPEF significantly affects the vertical $E \times B$ plasma drift. The large production-to-loss ratio at higher altitudes results into F-region electron density increase on the dayside. The resulting strong enhancement/depletion of total electron content (TEC) in the dayside/nightside is associated to PPEF (B Tsurutani, 2004; M A Abdu, 2007). Moreover, the influence of gravitational and pressure gradient forces moves equatorial plasma to higher latitudes and forms two crests on both sides of the magnetic equator, known as Equatorial Ionization Anomaly (EIA). The eastward/westward orientation of the PPEF drive forward and reverse plasma fountain effect (Duncan, 1960; T Kikuchi, 2008; C H Chen, 2008). Both amplitude and latitude of the EIA are intensified by PPEF (B Veenadhari, 2010). During geomagnetic storms, an increased Joule heating in the auroral zone can cause disturbances in thermospheric circulation and equatorward winds that results into a disturbance wind dynamo electric field (DDEF) (Blanc & Richmond, 1980). The DDEF originated from the perturbed neutral winds develop a few hours after the onset of the storm and it persists for several hours under the action of the thermospheric wind dynamo (Blanc & Richmond, 1980). The magnetic disturbances associated with the PPEF and DDFF are known as polar no. 2 (DP2) and ionospheric disturbance dynamo (Ddyn) current system, respectively (Nishida, 1968; Huy & Mazaudier, 2005). It is reported that a decrease in the amplitude of the Horizontal-component of the Earth's magnetic field at the magnetic equator is associated with Ddyn ((Huy & Mazaudier, 2005)). During quiet conditions, global scale neutral winds generate eastward electric currents in the altitude range between 100 and 130 km, known as the Solar quiet (Sq) wind dynamo. Within $\pm 2^{\circ}$ of the magnetic equator, an increased flow of this current system between altitudes 100 and 110 km is commonly known as the equatorial electrojet (EEJ) (Richmond, 1973b; Reddy, 1989; C H Chen, 2008). It is well known that westward EEJ is responsible for the decrease in the H-component of the Earth's magnetic field (Y Kassa & Tebabal, 2023).

The storm-induced ionospheric electron density enhancement or depletion is known as positive or negative ionospheric storms. It is demonstrated that a number of physical processes are responsible for electron density variations (B Nava, 2016; A Kashcheyev, 2018; G Prolss, 1991; Cole, 1966). The equatorward neutral wind can be the main driver of positive ionospheric storms at low and mid latitudes. The authors demonstrated that storm-time increase in oxygen density, a change in meridian winds which lifts the ionosphere to higher altitudes, traveling ionospheric disturbances (TIDs) and disturbed electric fields can play important role in plasma redistribution in the form of positive ionospheric storms. Moreover, the negative ionospheric storm can be attributed to storm induced changes in the atomic O/N_2 (N Balan, 2009; C S Huang & Michael, 2005).

The presence of ionospheric plasma irregularities in the equatorial-low-latitude can disturb the radio communication and navigation system (S Basu, 1999; A W Wernik & Fremouw, 2003). For this reason, the study of geomagnetic storm induced ionospheric plasma irregularities has received special attention of the space weather researcher. These irregularities are more prominent in the post-sunset and midnight equatorial/low latitude sectors due to the formation of equatorial plasma bubbles (EPBs). The lack of plasma production and fast recombination rate in E-region leads to sharp plasma density gradients in the post-sunset sector. Moreover, the enhanced F-region vertical plasma drift resulting from eastward electric field, is an important driver of these plasma irregularities. The vertical plasma drift moves the F-region to higher altitudes where the recombination rate is very slow. The resulting Rayleigh-Taylor (R-T) instability is responsible for the generation of equatorial/low-latitude plasma irregularities (B G Fejer, 1999). (P Amaechi, 2018) investigated the storms related ionospheric irregularities over the eastern and western African sector. The authors used magnetometers data to demonstrate that the variation in H and minima/oscillations in ionospheric electric current disturbance (Diono) are associated with PPEF during the main phase. Also, during the main phases of the March and October 2015 storms, the westward electric field suppressed plasma irregularities over the eastern sector. On the other hand, the eastward electric field triggered plasma irregularities over the same sector during the June 2015 storm. During the recovery phase, the dominating westward DDEF suppressed plasma irregularities.

Besides electric fields, the thermospheric winds play a vital role in the development of plasma irregularities, as for example, in the sunset equatorial sector, the F-layer ionosphere is affected by a pre-reversal enhanced (PRE) east-ward electric field and thus creating a R-T instability in the form of EPBs. According to (Abdu, 1997), storm-time energy deposition at high latitudes can affect global thermospheric circulation such as zonal and meridional winds, which can modify vertical plasma drifts, F-layer heights, and intensify the post-sunset irregularities (Rishbeth, 1971). However, meridional winds can effectively affect the global conductivity and the F layer gradients, thus inhibiting the generation of plasma irregularities (Maruyama, 1988). Based on TEC measurements, (B Nava, 2016) studied response of the middle and low latitudes ionosphere to the intense geomagnetic storm of March 2015 in America, Africa, and Asia longitude sectors. The authors have reported positive storm effect during the main phase and negative storm effects at at all longitude sectors for several days during the recovery phase of the storm. They also used spectral analysis of the magnetometer data to separate the effects of the convection electric field and of the disturbance dynamo. It was concluded that the short term oscillations (about 3 h periods) were related to DP2 fluctuations during southward IMF Bz and occurred simultaneously in the Asian, African, and American sectors. On the other hand, Ddyn showed local time differences for each longitude sector and lasted longer over the Asian followed by African and American sectors, respectively. (M Regi, 2022) studied the intense geomagnetic storm of November 3-6, 2021 through field line resonances and ionospheric parameters such as the critical frequency of the F2 layer, foF2 and TEC. The effects on the American sector as compared to the European sector were attributed to strong poleward meridional thermospheric wind in Europe. In this scheme, this study investigates the equatorial and low latitude ionospheric plasma irregularities that occur during the geomagnetic storm of 3-5 November 2021. Normally, the main phase of the geomagnetic storm triggers strong fluctuations and the recovery phase suppresses the occurrence of the equatorial plasma bubble irregularities. But here we will observe the inhibition of plasma irregularities during the main phase and their appearance during the recovery phase of the storm. We demonstrate the physical mechanisms that are responsible for the observed storm-time behaviour of the three longitudes. This article is organized as follows: Section 2 presents the data and analysis approach, and Section 3 contains the results and their descriptions. Finally, conclusions based on our findings are presented in Section 4.

2 Data and Methods

In this study, we employed the 1-minute time-resolution data of solar wind parameters, including the B_z component of the interplanetary magnetic field (IMF), the solar wind speed (V_{sw}), the interplanetary electric field (IEF), the proton density (n_p), the proton temperature (T_p), the solar wind pressure (P_{sw}), the Kp index and the $SYM-H$ index. The data is obtained from the NASA's OMNIWeb database (https://omniweb.gsfc.nasa.gov/).

The storm-time response of the ionosphere is assessed by analyzing TEC data from equatorial and low-latitude GPS receivers located in the Asian, African and American sectors. The global diurnal variation of the vTEC is estimated from the 15-minutes time resolution UPC GIM (UQRG) data available at (https://cddis.nasa.gov/archive/gnss/products/ionex/2021). In GIM, vTEC data is in standard ionosphere map exchange (IONEX) format for the entire globe. Each map contains approximately 5,184 data points (called GIM cells) with a spatial resolutions of 2.5° × 5° in geographic latitude and longitude.

The GPS-TEC data is converted into the rate of change of TEC index (ROTI). The ROTI is a proxy for ionospheric scintillation which can be estimated as the standard deviation of the rate of change of TEC at every 5-minute interval (Aarons, 1997; S Basu, 1999; X Pi, 1997);

$$\mathrm{ROTI} = \sqrt{<\mathrm{ROT}^2> - <\mathrm{ROT}>^2}, \tag{1}$$

where ROT is the time derivative of TEC,

$$\mathrm{ROT} = \frac{\mathrm{dTEC}}{\mathrm{dt}} = \frac{TEC(t_{k+1}) - TEC(t_k)}{t_{k+1} - t_k}. \tag{2}$$

Here dTEC is the difference in $\mathrm{TEC(t_{k+1})}$ and $\mathrm{TEC(t_k)}$ values at times $\mathrm{t_{k+1}}$ and $\mathrm{t_k}$, respectively. GPS-TEC software proposed by (Seemala, 2011) has been used to derive TEC from satellites with elevation angles $\geq 30°$ to minimize multi-path errors. TEC is measured in electrons per square meter and conventionally,

$$1\mathrm{TECU} = 10^{16}\mathrm{electrons/m^2}.$$

The unit of ROTI is TECU/min.

In order to estimate the effect of PEFs on ionospheric plasma irregularities, the temporal profile of the equatorial electric field over a specific longitude was obtained from the real-time PPEF model available at (https://geomag.colorado.edu/real-time-model-of-the-ionospheric-electric-fields). The model uses a transfer function to estimate the temporal variation of the equatorial ionospheric eastward electric field (EEF) with real-time solar wind data and a climatological model for the quiet EEF. The inputs are time and longitude, and it provides: the background quiet-time electric field, the PPEF, and the total electric field which is the sum of quiet-time and PPEF.

The storm-time response of the geomagnetic field is assessed by using 1-minute time resolution data from 3 low-latitude magnetometers located in 3 longitude sectors: Asia, Africa and America. In order to compute the resulting geomagnetic variations due to the storm, we use the approach adopted by (B Nava, 2016; A Kashcheyev, 2018). According to this approach, the horizontal component 'H' of the geomagnetic field can be expressed as:

$$\mathrm{H} = \mathrm{H_o} + \mathrm{D_m} + \mathrm{D_{iono}} + \mathrm{S_r^H}, \tag{3}$$

where $\mathrm{H_o}$ is the magnetic field component associated to Earth's external core, $\mathrm{D_m}$ is the disturbance due to the magnetospheric currents e.g. the Chapman Ferraro current, the ring current and the tail current. It can be estimated as:

$$\mathrm{D_m} = \mathrm{SYM-H} \times \cos\phi. \tag{4}$$

In this equation, ϕ is the geomagnetic latitude. In equation (3), $\mathrm{S_r^H}$ is the quiet daily regular variation calculated from 5 quietest days of November 2021 with $\mathrm{Kp} < 2$, and $\mathrm{D_{iono}}$ represents the disturbances related to the ionosphere. The $\mathrm{D_{iono}}$ can be expressed in simple form as:

$$\mathrm{D_{iono}} = \Delta\mathrm{H} - \mathrm{S_q} - \mathrm{D_m}. \tag{5}$$

In this equation, $S_q = < S_r^H >$ is the hourly amplitude of daily variations of the geomagnetic field. We further employ, a continuous wavelet transform to D_{iono} to detect different waves relevant to this study.

Finally, storm induced variations in the thermospheric neutral composition can be estimated through O/N_2. The Global Ultraviolet Imager (GUVI) onboard Thermosphere Ionosphere Mesosphere Energy and Dynamics (TIMED) satellite can provide a realistic estimate of O/N_2 (T Yu, 2020). The data is provided in grid format at (http://guvitimed.jhuapl.edu/data-products). The geographic coordinates of the GNSS receivers and magnetic observatories used in our analysis are presented in Table 1.

3 Results And Discussion

3.1 Solar Wind Parameters and Geomagnetic Indices:

The CME- driven geomagnetic storm of November 3-6, 2021 occurred during the ascending phase of the solar cycle 25. A halo CME was originated from M 1.7 class solar flare in the sunspot region AR2891 on November 2, 2021 at 03:00 Universal Time Coordinated (UTC). More information about this event is available at the National Oceanic and Atmospheric Administration (NOAA) Space Weather Prediction Centre (SWPC). According to NOAA SWPC, the arrival of the CME on Earth was detected at 19:42 UTC on November 3, 2021. The resulting geomagnetic response reached to G3 (Strong) storm level at 23:59 UTC preceded by G1 (Minor) and G2 (Moderate) storms at 21:24 and 21:46 UTC on November 3, 2021. The 1-minute time resolution datasets of solar wind parameters and IMF relevant to this space weather event are in Figure 1, where from top to bottom we have: the B_z component of the IMF, the solar wind speed (V_{sw}), the Ey component of the interplanetary electric field (IEF), the proton number density (n_p), the proton temperature (T_p), the solar wind pressure (P_{sw}), the Kp index and the SYM-H index. The red and magenta vertical dotted lines represent the arrival of the CME on Earth, which leads to the Sudden Storm Commencement (SSC) and the end of main phase, at 20:58 and 12:44 on November 3, and 4, respectively. The main phase began with a southward turning of the IMF B_z, reaching to a lowest value of approximately -17nT at 21:43 UTC on November 3, 2021. Then it rapidly increased to approximately +15.2 nT at 00:09 UTC on November 4, 2021. Afterwards, the IMF B_z turned southward again with a strong negative value -20.4 nT at 07:19 UTC until 12:44 UTC. Afterward, the B_z component increased gradually to normal values on November 5, 2021. Normal values of solar wind speed are about 332 km/s, and maximum values showed approximately 850 km/s at 11:39 UTC on November 4, 2021. The solar wind speed was altered during 3 days and returned to normal on November 7, 2021. Note, the IMF B_z changes polarity several times during the main phase of the storm. As a result, the IEF Ey also shows a similar fluctuations between -10.8 and 14.94 mV/m. The IEF Ey is estimated as $E_y = -B_z \times V_x$, where B_z is the Z component of the IMF and the V_x represents the X component of the solar wind speed. A positive (northward) IMF B_z generates a westward electric field on the dayside and eastward on the nightside. During the main phase of the storm, the proton density and temperature reach maximum values of 25 no./cm^3 and 10×10^5 K, respectively. The solar wind dynamic pressure $P_{sw} = m_p n_p V_{sw}^2$, exhibits a strong synergy with the IMF B_z. A notable enhancement in the dynamic pressure occurs under southward IMF B_z conditions with peak value of 28.54 nPa at 9:16 UT on November 4, 2021. The northward IMF B_z condition results into a weaker response of P_{sw}. The bottom plots in Figure 1, show the geomagnetic indices Kp and SYM-H. The Kp index shows a maximum value of approximately 8 on November 4, 2021 respectively. During the long southward turning of IMF B_z ($B_z < 0$), the magnetic re-connection between the IMF and the Earth's magnetic field drops the SYM-H index due to an enhanced ring current. The development of the double storm on November 4 show 2 minimum values of SYM-H of approximately -112 nT and -120 nT at 10:56 UTC and 12:44 UTC, respectively. The recovery phase started at 12:44 UTC with a northward turning of B_z and attained quiet normal conditions on November 6, 2021.

3.2 Ionospheric Response

Figure 2 shows the GIM based ionospheric vTEC and ΔvTEC over Asian, African and American sectors. The three longitude sectors show the following features during the main and the recovery phase of the storm:

- The Asian sector shows a regular pattern of vTEC with well-defined crests of vTEC, except on November 5, as shown in Figure 2a. On the day of the storm (November 4), the ΔvTEC shows a large increase of EIA with a clear latitudinal separation of the crests. We observe asymmetric distribution of vTEC in the north/south EIA crests. The ionization level is strong in the northern crest, reaching middle latitudes as compared to the southern crest. On the day after the storm (November 5), the ionization level in the crests decreases significantly, and an enhanced TEC is observed in the equatorial zone. The decrease in the vTEC is stronger in the southern crest region as compared to that observed in the northern crest region.
- The African sector exhibits a regular pattern of the vTEC with well-defined crests, except on the storm day (November 4). The ΔvTEC shows a strong increase in the equatorial zone and in the EIA region. Note an increase in vTEC at the northern high latitude. The day after the storm, the higher ionization level is confined to the equatorial zone and to the northern low latitude. Finally, note the increased ionization mostly disappears on the south side of the equator.
- On the storm day (November 5), the American sector exhibits a strong increase in vTEC in the equatorial zone, as well as in the northern low latitude. In the south American sector, the increase in the ionization level is expected to extend beyond 30° in latitude. The next day of the storm (November 5), the vTEC enhancement mostly occurs in the EIA crests region with a lower increase in vTEC in the equatorial zone.

Figure 3 presents the temporal variation of the vTEC recorded by the individual GNSS stations at the Asian, African and American sectors during the period 1 to 10 November 2021. Each panel contains the average quiet daily value (in blue) and the vTEC (in magenta). In Figure 3, the first 3 panels represent the southern low-latitude (MRO), the equatorial (BRUN) and the northern low-latitude (HKSL) stations in the Asian sector. At MRO, a large increase of vTEC is observed on the day of the storm. The day after the storm, the vTEC value drops to approximately 50% of its quiet time value at this station. At BRUN, the vTEC shows a small change in the ionization level during the storm phase. These observations are in agreement with the GIM of Asian sector presented in Figure 2. In Figure 3, the fourth to sixth panels show 3 GNSS stations in the African sector, MFKG (southern low-latitude), NKLG (equatorial) and MAS (northern low-latitude). At MFKG, we observe a large increase of vTEC on the day of the storm, which decreases significantly on the next day. NKLG shows an increase in the vTEC on the two consecutive days. These observations also agree with the GIMs of the African sector (Figure 2), indicating that the higher ionization level is confined to the equatorial zone. The Northern low-latitude station shows a little change in vTEC during November 3 to 5. In Figure 3, the seventh to ninth panels represent the three GNSS stations of the American sector, IQQ (southern low-latitude), QUI (equatorial) and SCUB (northern low-latitude). On the day of the storm, the three stations show a noticeable increase in vTEC, specially at the equatorial station.

Figure 4 shows the storm-time variation of the ROTI at several GNSS stations located in the equatorial and low-latitude stations of American, African, and Asian sectors. Note that the value of ROTI $>$ 0.5TECU/min indicates the presence of ionospheric irregularities at scale lengths of a few kilometres. The ionospheric irregularities can be classified as: weak ($0.25 < \text{ROTI} < 0.5$); moderate ($0.5 < \text{ROTI} < 1$) and strong ($\text{ROTI} > 1$) (Ma & Maruyama, 2005). Before the SSC (November 3, 2021), strong ionospheric irregularities can be observed over the equatorial and northern low latitude stations (**areq** and **bogt**) in the American sector. However, the ionospheric irregularities are very less pronounced at the south American station (**cord**). A significant latitudinal variation in the ionospheric irregularities can be seen within the same sector. In the African sector, we observe weak irregularities at **ykro**. In the Asian sector, **hksl** and **pimo** show lack of irregularities.

During the main phase of the storm (on November 4, 2021), the occurrence of ionospheric irregularities over equatorial and low-latitude stations is inhibited for all longitudes. During the early recovery phase of the storm (on November 5, 2021), the ionospheric irregularities appear at several stations, particularly in the equatorial and northern low latitude stations of the American sector. Note significant longitudinal differences in the occurrence of plasma irregularities during the storm recovery phase. Only the American sector exhibits noticeable irregularities during the night at the main phase of the storm. Clearly, the storm appeared not to hinder the development of plasma irregularities in the American sector. The generation of these irregularities can be associated with the eastward DDEF and/or an over-shielding PPEF. During the storm late recovery phase (on November 6, 2021), the occurrence of ionospheric irregularities is observed over the equatorial and low-latitude stations of American (**areq** and **bogt**) and African (**ykro** and **nklg**) sectors at different times. However, the occurrence of ionospheric irregularities is inhibited over the equatorial and low-latitude stations of the Asian sector during the main and recovery phases of the storm. It is well known that the Rayleigh Taylor (R-T) instability lead to the development of ionospheric irregularities which can be affected by external driving forces such as electric fields, magnetic field, and neutral winds (G Li, 2010, 2011). Storm induced ionospheric irregularities also depend on season, local time, gravity waves, etc. We suspect the presence (absence) of ionospheric irregularities over the three longitude sectors (American, African and Asian) before the storm initial phase ($\text{Kp} < 4$) can be related to a seasonal dependence. Over the American sector, strong ionospheric irregularities usually occur in December solstice (Y Sahai, 1994). On the other hand, December solstice is non-occurrence season of irregularities at the African and Asian sectors. The inhibition of ionospheric irregularities during the main phase of the storm at specific longitudes can be partly attributed to storm timing. The main phase of the storm occurred between 21:30 UT (on 3 November) and 12:44 UT (on 4 November). During this phase, we have local dawn-to-sunset hours in Asian sector, the local night-to-noon hours in African sector and the local evening-to-night hours in the American sector. (Aarons, 1991) reported that the ring current during geomagnetic storms play a leading role in establishing necessary conditions for generation or inhibition of plasma irregularities. The authors discussed local time dependence of the ring current during maximum excursion of the SYM-H and transmission to the equatorial electric field, which is reflected in variations of F layer height. Moreover, the authors stated that the maximum excursion of the storm main phase occurred after sunset or shortly after sunset, with insignificant effect on the development of irregularities at night. If the maximum negative SYM-H excursion occurs in the afternoon, the ionospheric irregularities would be inhibited. On the other hand, a maximum excursion of SYM-H during local midnight to post midnight supports the generation of ionospheric irregularities. Therefore, the lack of ionospheric irregularities during the storm main phase over the African sector is consistent with the Aaron's criteria. However, the suppression of plasma bubble occurrence over American and Asian sectors during the main phase of the storm could not be explained by Aaron's criteria. Lee et al. (2005) suggested a lack of ionospheric irregularities could be explained through the effect of geomagnetic activity on $\text{E}\times\text{B}$ drift. Several researchers (C Martinis & Aarons, 2005; Oladipo & Schüler, 2014; T Dugassa, 2019) suggested geomagnetic storms may enhance or suppress the development of ionospheric irregularities. Over the equatorial and low-latitude region, since the magnetic field orientation is unique, the equatorial/low-latitude ionosphere is sensitive to changes in electric fields. PPEF and DDEF are the main sources that modulate the electromagnetic environment, hence, these affect the occurrence of ionospheric irregularities. It can be expected that over-shielding electric field (westward PPEF) associated with the rapid oscillation of IMF Bz may hinder the occurrence of ionospheric irregularities by suppressing the upward motion of F-layer (T Kikuchi, 2008; B G Fejer, 1999).

During geomagnetic storms, the dawn-to-dusk convection electric field generated at the high latitude can cause the under-shielding PPEF to penetrate into equatorial/low-latitudes, thus modify the quiet time electric field pattern (Buonsanto, 1999). A westward (or eastward) electric field during the nighttime (or daytime) may suppress (or favor) the upward drift of a plasma. The injection of westward electric fields during the main phase must hinder the normal upward plasma drift and impede the development of irregularities. These differences during the first night following the recovery of the storm (Figure 4) can be explained in term of longitudinal dependence of storm induced disturbance dynamo mechanism (G Li, 2011). The scenario in the African and Asian sectors are different compared to the observations in the American sector. The storm activity appear to hinder the development of irregularities during the first night, following the recovery phase, as observed in Figure 4.

PPEFM is used to obtain storm-time behaviour of PEFs over the three longitude sectors, as shown in Figure 5. This figure shows (a) the background quiet-time electric field (in black); (b) the PEFs(in magenta); and (c) the total electric field, as the sum of quiet-time and PEFs (in blue). The injection of PEF into the low-latitude during the main phase of the storm occurred between the local midnight and around the noon in the African sector. Following our hypothesis, it is suspected that this time may not be favourable for the occurrence of the plasma irregularities in the African sector. The injection of PEFs may inhibit the diffusion of plasma, causing instability with a consequent lack of irregularities. Over the Asian sector, PEF is injected into the low-latitude during the initial phase after sunset. (T Dugassa, 2019) showed a longitudinal variability in the occurrence of ionospheric irregularities during intense geomagnetic storms in the equatorial and low-latitude regions of America, Africa, and Asia. It was found that the local time occurrence of the maximum negative excursion of the SYM-H index and the electric field play important role in the observed longitudinal variability of the ionospheric irregularities. The lack of ionospheric irregularities observed at night during the recovery phase day (November 5, 2021) in the African can be associated with other storm related drivers that may oppose the upward motion of plasma (O S Bolaji, 2019). These drivers may include the action of (a) westward PEFs due to northward orientation of the IMF B_z during the recovery phase, and (b) the DDEF due to storm induced equatorward wind. The lack of irregularities in the stations over the African and Asian regions may be an evidence of the disturbance dynamo mechanism on November 5, 2021.

Storm-time neutral winds play an important role in the generation of ionospheric irregularities. In this context, Figure 6 shows the global maps of O/N_2 ratio from GUVI TIMED during the period November 3-6, 2021. These maps show different pattern of O/N_2 ratio on geomagnetically disturbed days (November 3-6, 2021). Previous studies have shown that O/N_2 is a key parameter to assess the impact of thermospheric composition on plasma density variation (B Nava, 2016). With the development of the geomagnetic storm, the O/N_2 ratio shows strong depletion in the polar cap regions and expands non uniformly over different longitudes. The equator-ward O/N_2 depletion from high latitudes indicates an equator-ward movement of a neutral composition disturbance characterized by molecule rich gas induced by heating and upwelling (T J Fuller-Rowell, 1994). In particular, on November 4, the O/N_2 depletion in north Pacific and in north America expands to low latitudes. Note about 75% increment in O/N_2 in the equatorial zone that expands 15° north in the American sector. In south America, the depression of the O/N_2 ratio appears from the auroral zone to middle latitudes on the storm day. Note also a 20% increase in the O/N_2 ratio occurs at low latitude on the south side of the magnetic equator in these Pacific and American sectors. The quiet time pattern of the O/N_2 ratio is relatively a constant value of approximately 0.6 in the EIA and equatorial regions of the Africa sector. This pattern changes significantly with the development of the storm. On November 4, the O/N_2 ratio increases up to 75% between latitudes 28° and 35° in north Africa, with approximately 30% increase in the equatorial zone. The south side of the magnetic equator also shows a slight increase in the O/N_2 ratio with a weak depletion observed between latitudes 25° and 35° on this day. A day after the storm (November 5), the depletion of the O/N_2 ratio in south Africa becomes stronger and reaches 15S°. In the Asian sector, a 60% increase in the O/N_2 ratio can be observed in the middle latitudes during the storm period. On the other hand, the lower latitudes and equatorial zone show lack of enhancement.

The equator-ward expansion of the neutral composition disturbance depends on season and local time (T J Fuller-Rowell, 1994; G Prolss, 1991). In the summer hemisphere (in this case the southern hemisphere), the minimum ion drag and unidirectional winds (both summer-winter and storm-driven winds) are favorable conditions for easy transmission of the neutral composition perturbations to low latitudes during the night. The observation of the storm-time increase in O/N_2 ratio coincides with the storm-time TEC enhancement in the low latitudes.

3.3 Geomagnetic Field Response

In Figure 7, the temporal variation of the horizontal component of the Earth's field H(blue), the quiet daily variation S_q (black), and the disturbed electric current D_{iono} are presented for the three longitudinal sectors. The first common pattern is the sharp increase in the strength of the magnetic field at the SSC. The observed global increase in the field strength during the compression of the magnetosphere is explained by the Chapman current (Chapman & Ferraro, 1931). The second global feature is a strong decrease associated with the growth of the ring current during the main phase of the storm. Then, the recovery phase begins due to gradual decay of the ring current with the north-ward turning of the IMF B_z. Note the minimum value of H component with a peak of approximately -227 nT at the station DLT in the Asian sector. Minimum values of -128 nT and -80 nT are recorded at TAM (Africa) and KOU(America) at different local times. The storm recovery takes three days to turn back to normality.

In our last analysis, we employ the wavelet transformation with D_{iono} to obtain a complete picture of the periodicities associated with the disturbances. The wavelet power spectrum (WPS) of D_{iono} is presented in Figure 8, showing from top to bottom, the Asian, African and American sectors. For each station, the values are normalized on a scale of 0(black) to 10(bright). We observe short-term oscillations (period less than 4 h) and long-term oscillations (period between 12 h to 24 h) during the storm period. The short-term oscillations are recorded by the magnetometers on the day of the storm. An increase in the power of periods between 2 hr and 4 hr during the main phase is evident on the magnetometers in the Asian (DLT) and African(TAM) sectors. Also, short-term oscillations are present during the period from 3 to 6 November 2021. Long-term oscillations, on the other hand, show highest increase in the power of periods of approximately 10 hr, 12 hr and 24 hr.

4 Conclusion

We investigated the impact of the intense geomagnetic storm of November 3-6, 2021 on equatorial and low-latitude ionosphere over Asia, Africa and America. The study is based on the analysis of datasets obtained from multiple instruments including GNSS receivers, magnetometers and in situ measurements of different spacecraft missions. Following are the main conclusions of this study:

- A positive (enhanced TEC) ionospheric storm is observed during the main phase of the storm on November 4, 2021 over Asian, African and American sectors. The

Table 1. Information of the GNSS and Magnetometer stations used in the analysis.

Instrument Type	Station	Sector	Geographic Latitude	Geographic Longitude
GNSS	MRO	Asia	$26.70°S$	$116.64°E$
GNSS	BRUN	Asia	$4.97°N$	$114.95°E$
GNSS	PIMO	Asia	$14.64°N$	$121°E$
GNSS	HKSL	Asia	$22.37°N$	$113.93°E$
GNSS	MFKG	Africa	$25.81°S$	$25.54°E$
GNSS	YKRO	Africa	$6.86°S$	$5.24°W$
GNSS	NKLG	Africa	$0.35°N$	$9.67°E$
GNSS	DJIG	Africa	$11.53°N$	$42.85°E$
GNSS	MAS	Africa	$15.63°N$	$15.63°W$
GNSS	CORD	America	$31.53°S$	$64.47°$
GNSS	IQQ	America	$20.27°S$	$70.13°W$
GNSS	AREQ	America	$16.46°S$	$71.49°W$
GNSS	QUI	America	$0.14°N$	$78.47°W$
GNSS	BOGT	America	$4.64°N$	$74.08°W$
GNSS	SCUB	America	$20.01°N$	$75.70°W$
Magnetometer	DLT	Asia	$11.94°N$	$109.1°E$
Magnetometer	TAM	Africa	$5.53°N$	$22.79°W$
Magnetometer	KOU	America	$5.91°N$	$52.93°W$

storm-time increase of plasma density reached the mid-latitudes in the Asian sector as a result of the poleward EIA extension. Negative (TEC depletion) storm conditions are prominent over the Asian sector during the recovery phase of the storm on November 5, 2021. Factors such as thermospheric composition variability, equator-ward neutral winds, and PPEFs play important roles in the generation of positive ionospheric storms. In the absence of an electric field, the storm-driven winds play an important role for a plasma density enhancement.

- The suppression of ionospheric irregularities are observed in the three sectors during the main phase of the storm. The occurrence of ionospheric irregularities are detected over American and African sectors during the recovery phase of the storm. The strength of plasma irregularities is strong over American sector as compared to the African sector. The longitudinal variability in the development/inhibition of ionospheric irregularities during geomagnetic storm are potentially associated with local time occurrence of maximum ring current and the injection of PEFs during different phases of the storm.
- The geomagnetic field variations also reveal local time effects associated with daytime electric currents. The decrease in the H component of the Earth's magnetic field shows longitudinal variation. The strong decrease is observed in Asian sector followed by African and American sectors. D_{iono} also shows longitudinal variation during on the storm day. The American sector (nightside) exhibits a large positive value of D_{iono} during the main phase. However, the dayside sectors show negative value of the D_{iono} during this phase. The Wavelet Power Spectrum variation of the magnetometer stations shows stronger amplitudes in Asia and Africa with shorter periods approximately 3-4 hr. The three sectors exhibit stronger amplitude with periods 11-12 hr and 24 hr during the storm.

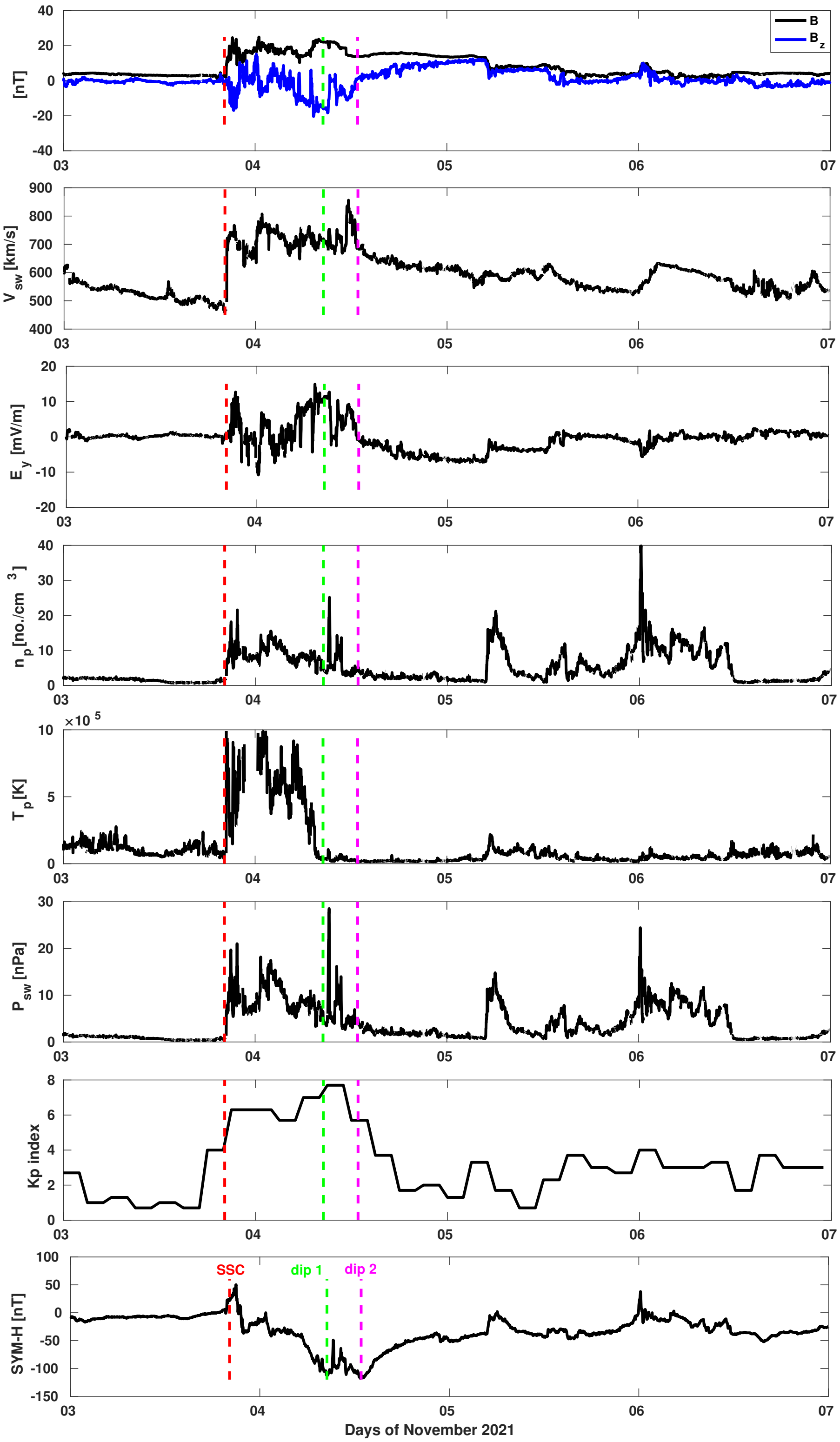

Figure 1. Solar wind parameters during CME driven storm of November 3-6, 2021.

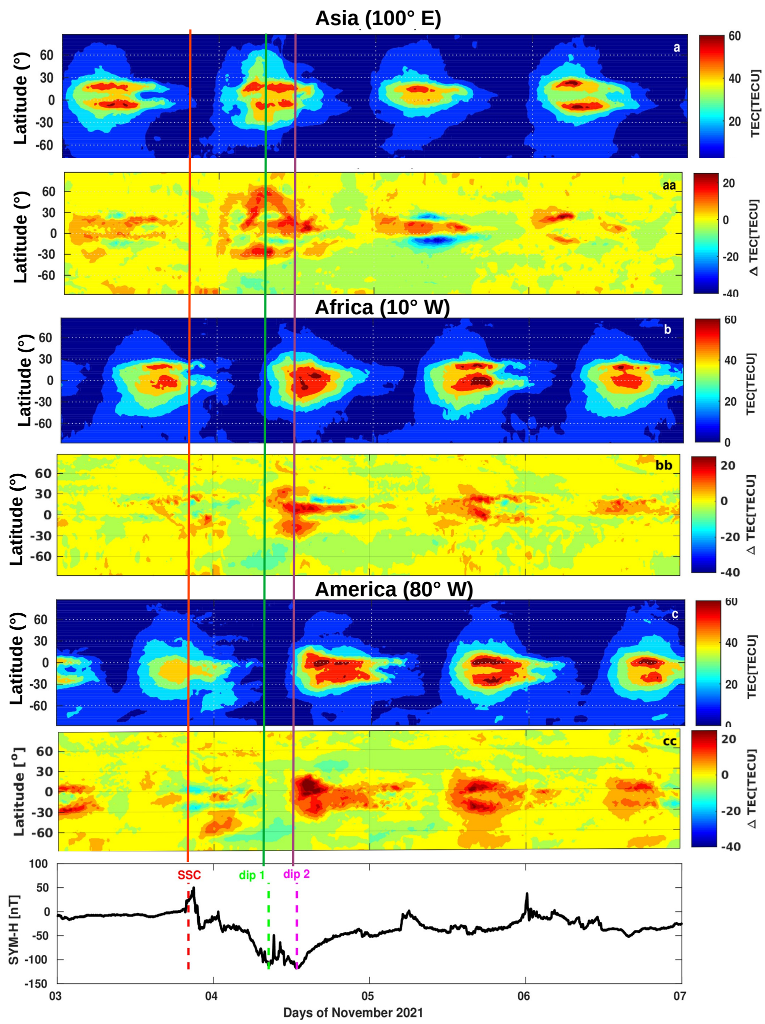

Figure 2. GIM-based distribution of TEC (in panel a, b and c), the deviations of TEC (ΔTEC) with the reference values (in panel aa, bb and cc) over Asia, Africa, America, and the SYM-H index (bottom) during the CME driven storm of November 3-6, 2021.

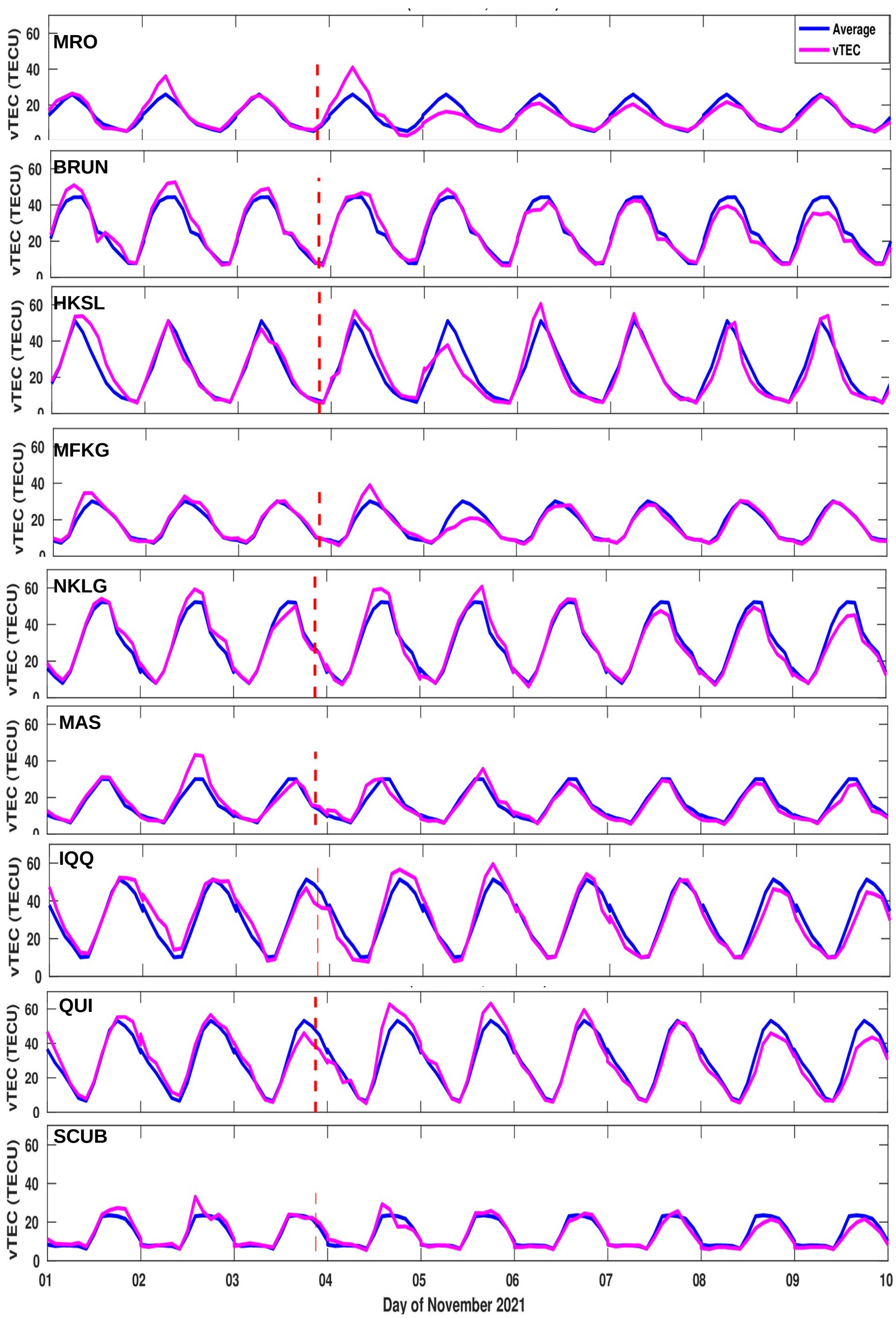

Figure 3. Vertical Total Electron content variation over the Asian, the African and the American sectors during the CME driven storm of November 3-6, 2021. Each panel shows the disturbed vTEC (in magenta) and the average quiet value (in blue).

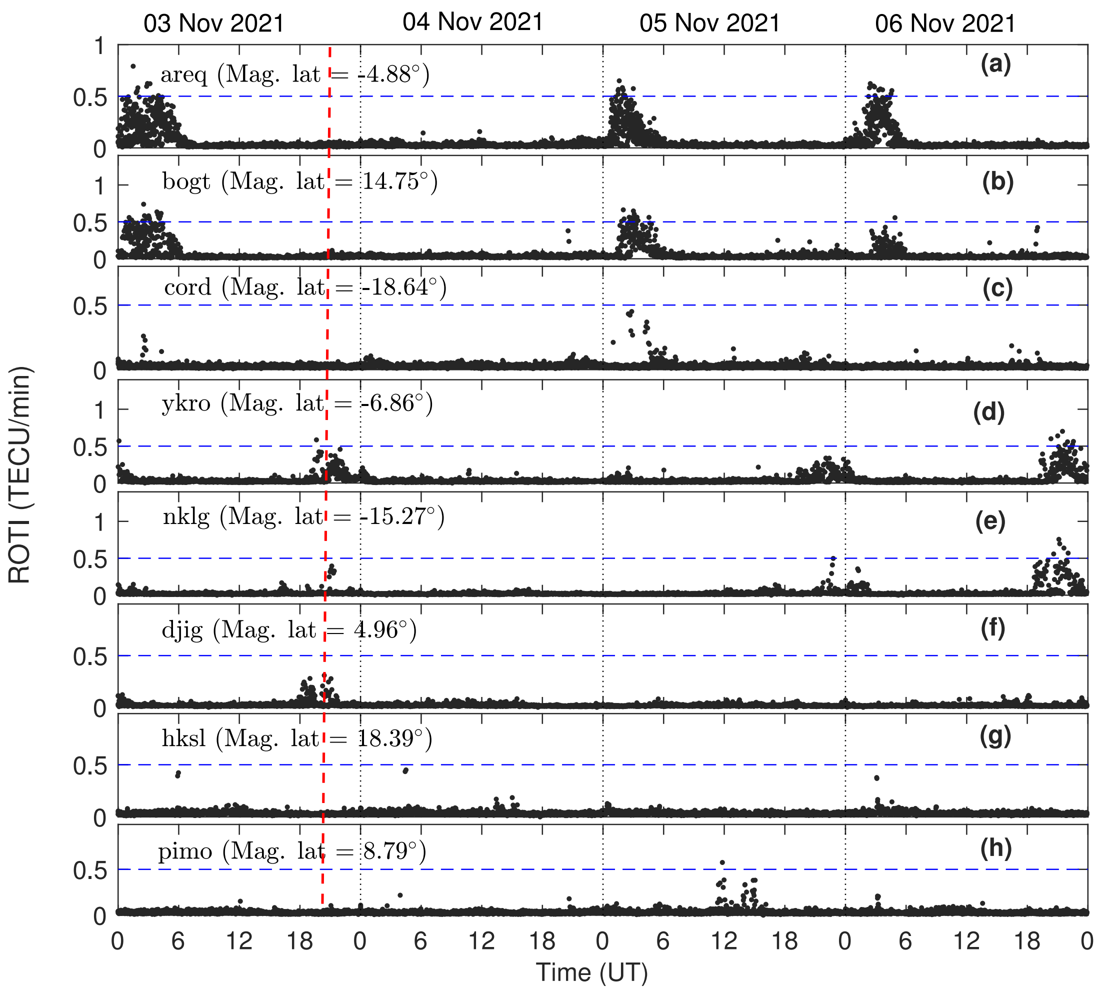

Figure 4. Diurnal variation of the Rate of TEC index (ROTI) at specific longitude in Asian, African, and American sectors during the CME driven storm of November 3-6, 2021.

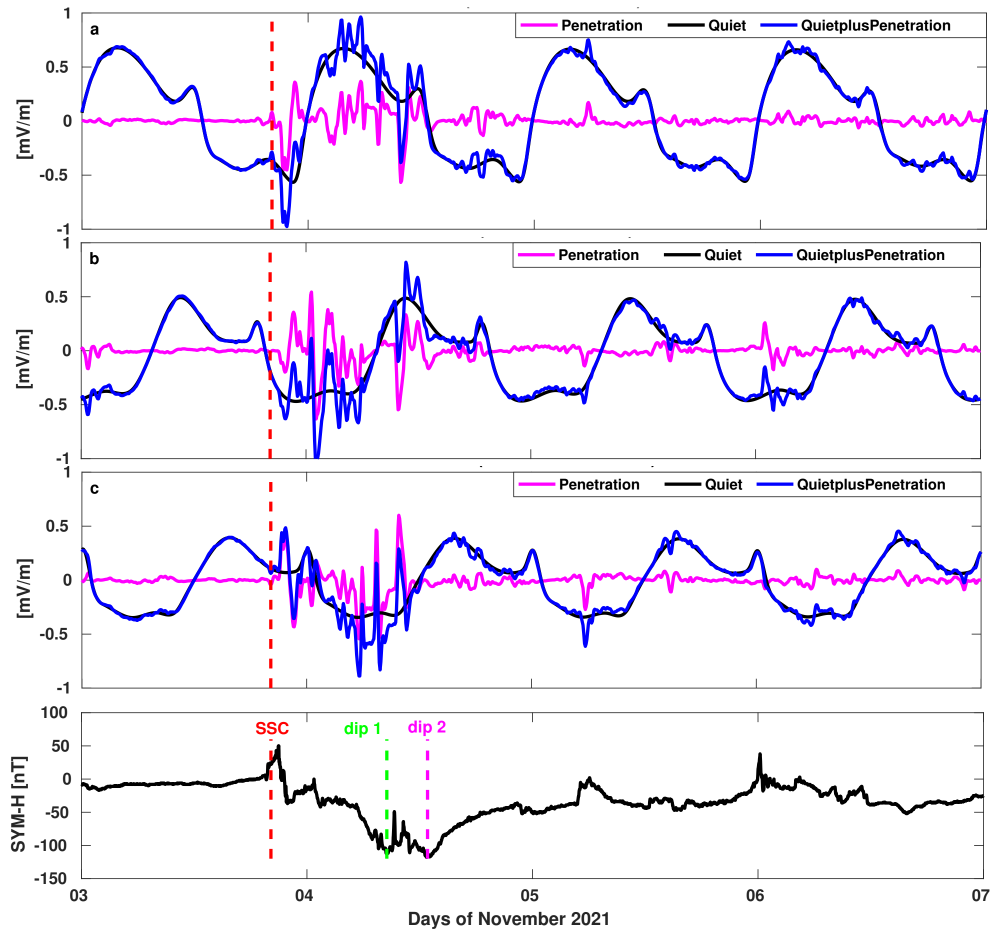

Figure 5. Temporal variation of the prompt penetration electric field for Asian (panel a), African (panel b) and American (panel c) sectors, and the bottom plot represents the SYM-H index during the CME driven storm of November 3-6, 2021.

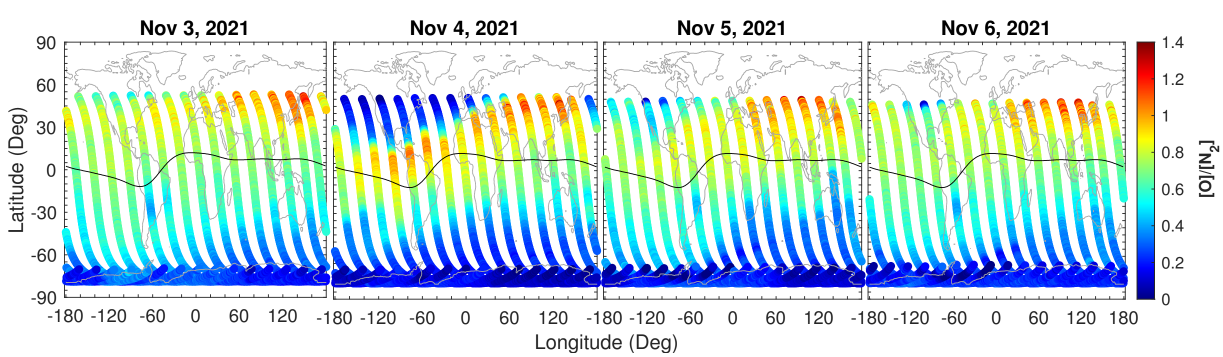

Figure 6. Global maps of O/N_2 composition during the period November 3-6, 2021 obtained from GUVI-TIMED. The black line represents the geomagnetic equator.

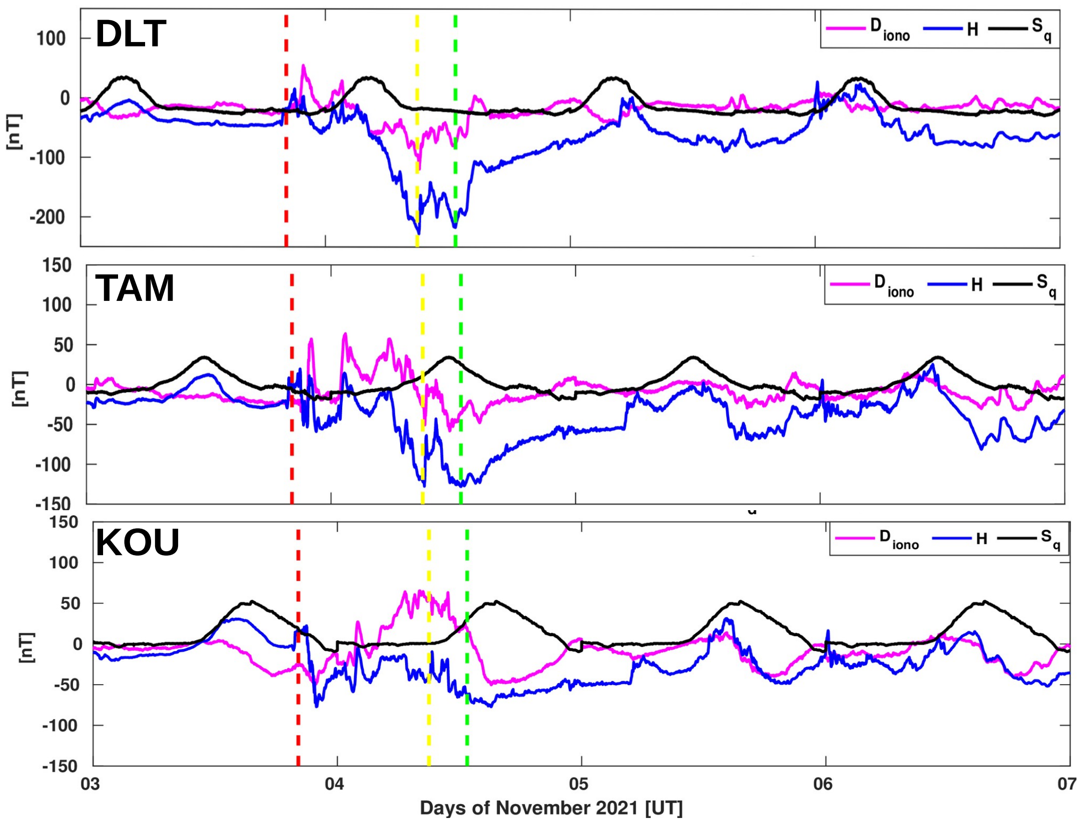

Figure 7. Magnetic field variation at specific longitude in Asian, African and American sectors during the CME driven storm of November 3-6, 2021.

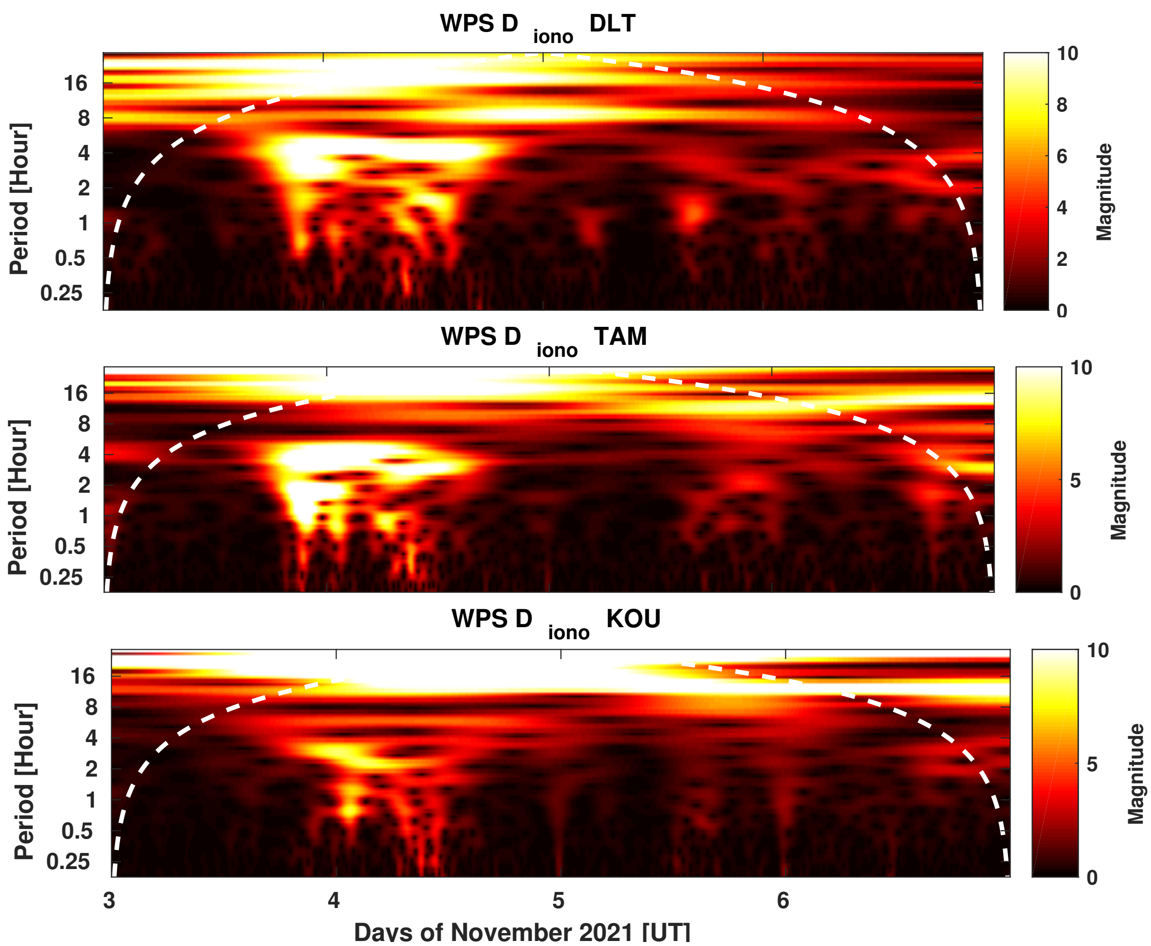

Figure 8. Wavelet Power Spectrum variation of D_{iono} at specific longitude in Asian, African and American sectors during the CME driven storm of November 3-6, 2021.

Acknowledgments

We acknowledge the following data portals:// the solar wind parameters and magnetic indices are available at NASA OMNI website (http://omniweb.gsfc.nasa.gov/, accessed on 2022) and at the ISGI website (http://isgi.unistra.fr, accessed on 2022). The magnetometer data are available at the INTERMAGNET website (https://www.intermagnet.org/, accessed on 2022). The IGS GIMs TEC are available at https://igs.org/data-products-overview/. Special thanks are given to the anonymous reviewers for helping to improve the manuscript.

References

Aarons, J. (1991). The role of the ring current in the generation or inhibition of equatorial f layer irregularities during magnetic storms. *Radio Sci.*, *26*(8), 1131–1149.

Aarons, J. (1997). Global positioning system phase fluctuations at auroral latitudes. *Geophys. Res.: Space Phys.*, *102*, 17219-17231.

A Balogh, e. a., V Bothmer. (1999). The solar origin of corotating interaction regions and their formation in the inner heliosphere. *Space Sci. Rev.*, *89*(1), 141–178.

Abdu, M. A. (1997). Major phenomena of the equatorial ionosphere-thermosphere system under disturbed conditions. *Atmospheric and Solar-Terrestrial Physics*, *59*(13), 1505–1519.

A Calabia, e. a., C Anoruo. (2021). Low-latitude ionospheric responses and coupling to the february 2014 multiphase geomagnetic storm from gnss, magnetometers, and space weather data. *Atmosphere*, *13*.

A Kashcheyev, e. a., Y Migoya-Orué. (2018). Multi-variable comprehensive analysis of two great geomagnetic storms of 2015. *Geophys. Res.*, *123*.

A K Singh, e. a., A Bhargawa. (2021). Physics of space weather phenomena: A review. *Geosciences*, *11 (286)*.

A W Wernik, J. A. S., & Fremouw, E. J. (2003). Ionospheric irregularities and scintillation. *Advances in Space Research*, *31*(4), 971-981.

B G Fejer, E. R. d. P., L Scherliess. (1999). Effects of the vertical plasma drift velocity on the generation and evolution of equatorial spread f. *Geophys. Res.*, *104*.

Blanc, M., & Richmond, A. D. (1980). The ionospheric disturbance dynamo. *Geophys. Res.*, *85*.

B Nava, e. a., J R Zuluaga. (2016). Middle and low-latitude ionosphere response to 2015 st. patrick's day geomagnetic storm. *Geophys. Res.*, *121*.

B Tsurutani, e. a., A Mannucci. (2004). Global dayside ionospheric uplift and enhancement associated with interplanetary electric field. *Geophys. Res.*, *109*.

B T Tsurutani, e. a., C M Ho. (1995). Large amplitude imf fluctuations in corotating interaction regions: Ulysses at mid-latitudes. *Geophysical Research Letters*, *22(23)*.

Buonsanto, M. J. (1999). Ionospheric storms-a review. *Space Sci. Rev.*, *88*(3-4), 563–601.

B Veenadhari, e. a., S Alex. (2010). Penetration of magnetospheric electric fields to the equator and their effects on the low-latitude ionosphere during intense geomagnetic storms. *Geophys. Res.*, *115*.

Chapman, S., & Ferraro, V. C. A. (1931). New theory of magnetic storms. *Terr. Magnetosphere Atmosphere Electr.*, *36*, 77–97.

C H Chen, e. a., J Y Liu. (2008). Equatorial ionization anomaly of the total electron content and equatorial electrojet of ground-based geomagnetic field strength. *Atmospheric and Solar-Terrestrial Phys.*, *70*(17).

C Martinis, M. M., & Aarons, J. (2005). Toward a synthesis of equatorial spread f onset and suppression during geomagnetic storms. *Geophys. Res.: Space Phys*, *110*.

Cole, K. D. (1966). Magnetic storms and associated phenomena. *Space Sci. Rev.*, *5*.

C S Huang, J. F., & Michael, K. (2005). Long-duration penetration of the interplanetary electric field to the low-latitude ionosphere during the main phase of magnetic storms. *Geophysical Research*, *110*.

Dalton, J. (1834). Meteorological observations and essays. , *2*.

Duncan, R. A. (1960). The equatorial f-region of the ionosphere. *Atmospheric and Terrestrial Physics*, *18*.

Feynman, J., & Crooker, N. U. (1978). The solar wind at the turn of the century. *Nature*, *275*.

G Li, e. a., B Ning. (2010). Longitudinal development of low-latitude ionospheric irregularities during the geomagnetic storms of july 2004. *Geophys. Res.*, *115(A4)*.

G Li, e. a., B Ning. (2011). On the occurrence of post-midnight equatorial f region irregularities during the june solstice. *Geophys. Res.*, *116*(376).

Gopalswamy, N. (2004). A global picture of cmes in the inner heliosphere.

Gopalswamy, N. (2006). Coronal mass ejections of solar cycle 23. *Astrophys. and Astron.*, *27*(2).

G Prolss, e. a., L Brace. (1991). Ionospheric storm effects at subauroral latitudes: A case study. *Geophysical Research*, *96(A2)*.

Huy, L., & Mazaudier, C. (2005). Magnetic signature of the ionospheric disturbance dynamo at equatorial latitudes: “ddyn”. *Geophys. Res.*, *110*.

J T Gosling, e. a., D J McComas. (1991). Geomagnetic activity associated with earth passage of interplanetary shock disturbances and coronal mass ejections. *Geophys. Res.: Space Physics*, *96(A5)*.

Lakhina, G. S., & Tsurutani, B. T. (2016). Geomagnetic storms: historical perspective to modern view. *Geosci. Lett.*, *3*(5).

Ma, G., & Maruyama, T. (2005). A super bubble detected by dense gps network at east asian longitudes. *Geophys. Res. Lett.*, *33*.

M A Abdu, e. a., T Maruyama. (2007). Ionospheric responses to the october 2003 superstorm: Longitude/local time effects over equatorial low and middle latitudes. *Geophys. Res.*, *112*, A10306.

Maruyama, T. (1988). A diagnostic model for equatorial spread f , 1, model description and application to electric. *Geophys. Res. Lett.*, *93(A12)*.

M J Owens, M. L. e. a. (2021). Extreme space-weather events and the solar cycle. *Solar Phys.*, *296*(82).

M Neugebauer, B. E. G., R Goldstein. (1997). Features observed in the trailing regions of interplanetary clouds from coronal mass ejections. *Geophys. Res.: Space Physics*, *102(A9)*.

M Regi, e. a., L Perrone. (2022). Space weather effects observed in the northern hemisphere during november 2021 geomagnetic storm: The impacts on plasmasphere, ionosphere and thermosphere systems. *Remote Sens.*, *14*.

N Balan, e. a., H Alleyne. (2009). Relative effects of electric field and neutral wind on positive ionospheric storms. *Earth Planet Sp*, *61*(439–445).

Nishida, A. (1968). Geomagnetic dp2 fluctuations and associated magnetospheric phenomena. *Geophys Res.*, *73*.

N M Pedatella, e. a., J Lei. (2009). Observation of the ionospheric response to the 15th december 2006 geomagnetic storm: Long duration positive storm effect. *Geophys. Res.*, *114*.

Oladipo, O. A., & Schüler, T. (2014). Magnetic storm effect on the occurrence of ionospheric irregularities at an equatorial station in the african sector. *Annals Geophys.*, *56*.

O S Bolaji, J. B. F., S J Adebiyi. (2019). Characterization of ionospheric irregularities at different longitudes during quiet and disturbed geomagnetic conditions. *Atmospheric and Solar-Terrestrial Physics*, *182*.

P Amaechi, A. A., E Oyeyemi. (2018). Geomagnetic storm effects on the occurrences of ionospheric irregularities over the african equatorial/low latitude region. *Advances in Space Research*, *61*.

Reddy, C. (1989). The equatorial electrojet. , *PAGEOPH 131*.

Richmond, A. D. (1973b). Equatorial electrojet-ii. use of the model to study the equatorial ionosphere. *Atmos. Terr. Phys*, *35*.

Richmond, A. D., & Matsushita, S. (1975). Thermospheric response to a magnetic substorm. *Geophys. Res.*, *80 (19)*.

Rishbeth, H. (1971). Polarization fields produced by winds in the equatorial f-region. *Planetary and Space Science*, *19(3)*.

Sabine, E. (1852). On periodical laws discover-able in the mean effects of the larger magnetic disturbance. no. ii. phil. trans. roy. soc. london. , *142*.

S Basu, e. a., K Groves. (1999). A comparison of tec fluctuations and scintillation at ascension island. *J. Atmos. Solar Terr. Phys.*, *61*, 1219–1226.

Seemala, G. (2011). Gps-tec analysis application. *Technical Report. Tech. Rep., Inst. for Sci. Res., USA*.

T Dugassa, M. N., J B Habarulema. (2019). Longitudinal variability of occurrence of ionospheric irregularities over the american, african and indian regions during geomagnetic storms. *Adv. Space Res.*, *63*.

T J Fuller-Rowell, e. a., M V Codrescu. (1994). Response of the thermosphere and ionosphere to geomagnetic storms. *Geophys. Res.*, *99*(A3).

T Kikuchi, K. N., K K Hashimoto. (2008). Penetration of magnetospheric electric fields to the equator during a geomagnetic storm. *Geophys. Res.*, *113*(A06214).

T Yu, e. a., Z Ren. (2020). Comparison of reference heights of o/n2 based on guvi dayside limb measurement. *Geophys. Res.*, *18*.

W D Gonzalez, e. a., J A Joselyn. (1994). What is a geomagnetic storm. *Geophys. Res.*, *99(A4)*.

X Pi, e. a., A Mannucci. (1997). Monitoring of global ionospheric irregularities using the worldwide gps network. *Geophys. Res. Lett.*, *24*.

Y Kamide, e. a., W Baumjohann. (1998). Current understanding of magnetic storms: Storm-substorm relationships. *Geophys. Res.*, *103(A8)*(17).

Y Kassa, B. D., & Tebabal, A. (2023). Ionospheric and magnetic signatures of extreme space weather events of 17 march and 23 june 2015 over the african sector. *Atmospheric and Solar-Terrestrial Physics*, *243*, 106003.

Y Sahai, e. a., J Aarons. (1994). Oi 630 nm imaging observations of equatorial plasma depletions at 16°s dip latitude. *Atmos. Terr. Phys.*, *56 (11)*.

Figure 1.

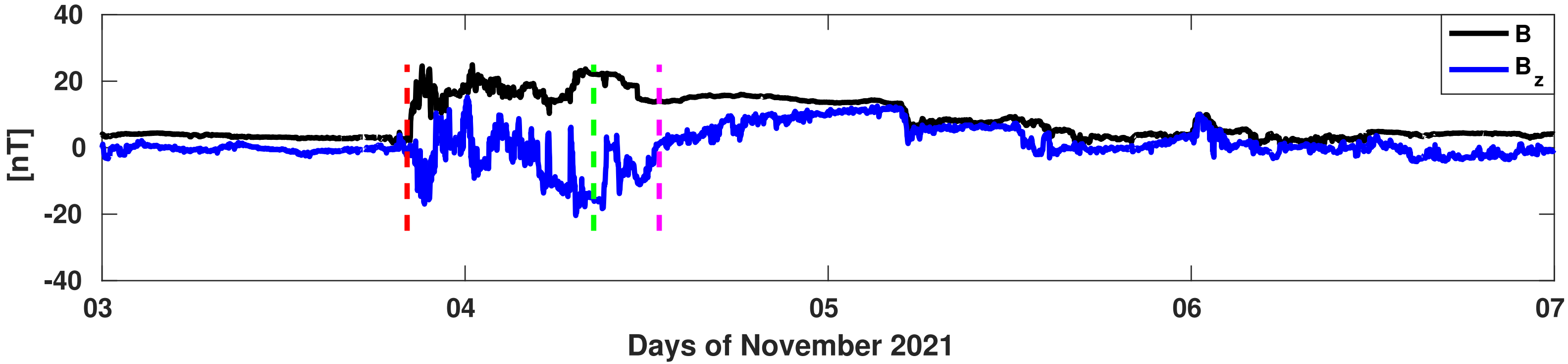

40
20
0
-20
-40
[nT]
B
B_z
03
04
05
06
07
Days of November 2021

Figure 1.

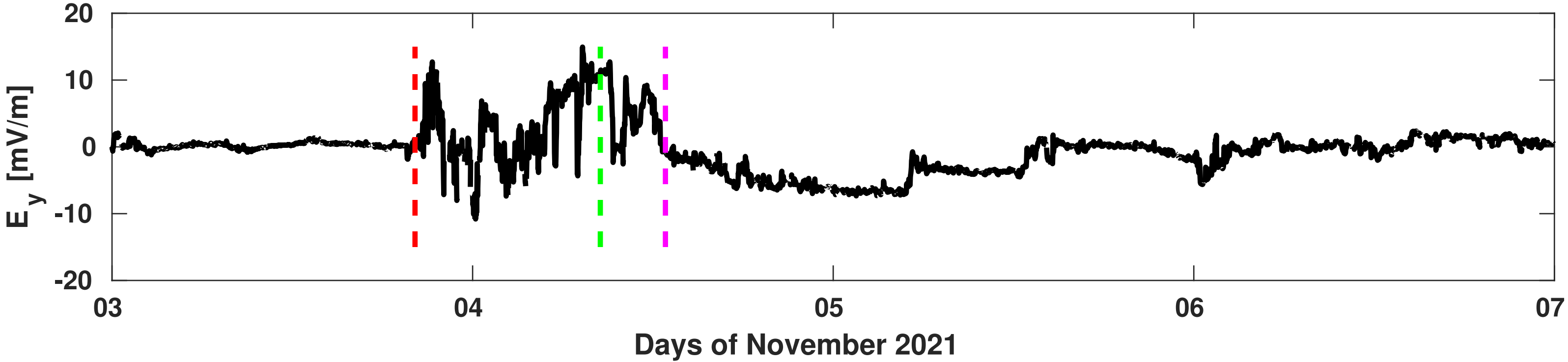
20
10
0
-10
-20
E_y [mV/m]
03
04
05
06
07
Days of November 2021

Figure 1.

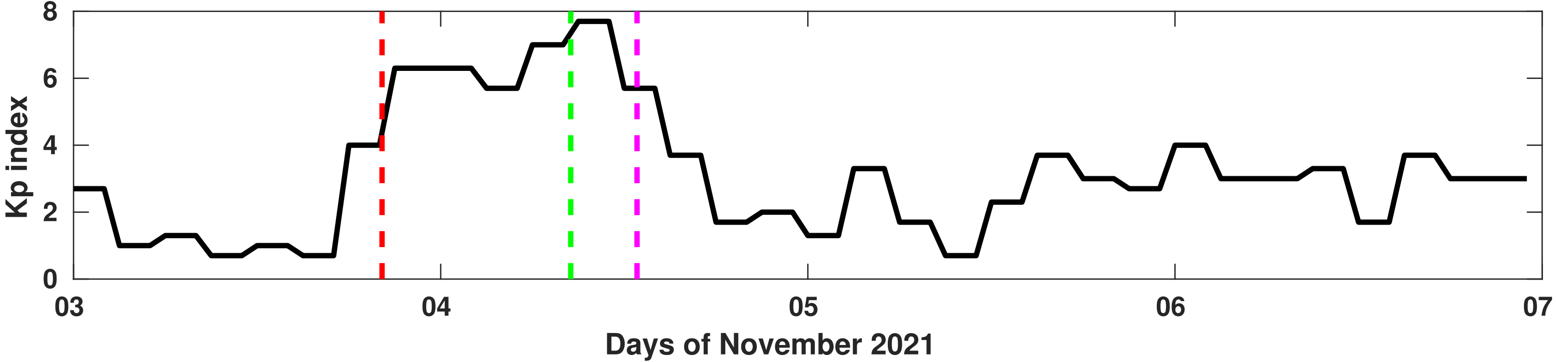

Kp index
8
6
4
2
0
03
04
05
06
07
Days of November 2021

Figure 6.

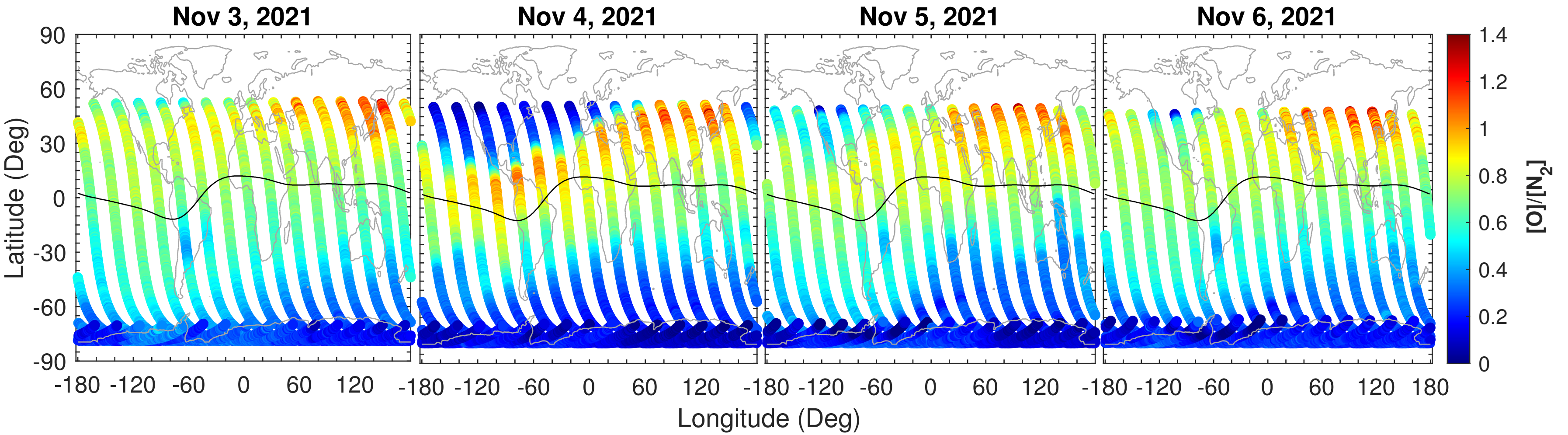

Nov 3, 2021
Nov 4, 2021
Nov 5, 2021
Nov 6, 2021
Latitude (Deg)
90
60
30
0
-30
-60
-90
-180 -120 -60 0 60 120
Longitude (Deg)
[O]/[N$_2$]
1.4
1.2
1
0.8
0.6
0.4
0.2
0

Figure 5.

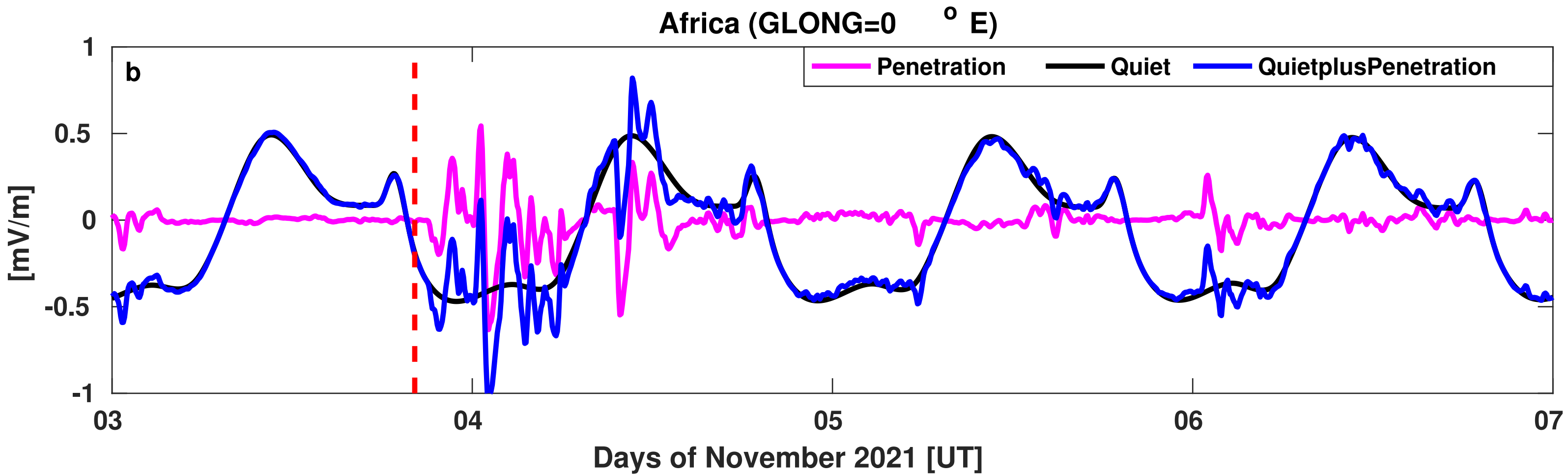

Africa (GLONG=0 o E)
b
Penetration
Quiet
QuietplusPenetration
[mV/m]
1
0.5
0
-0.5
-1
03
04
05
06
07
Days of November 2021 [UT]

Figure 5.

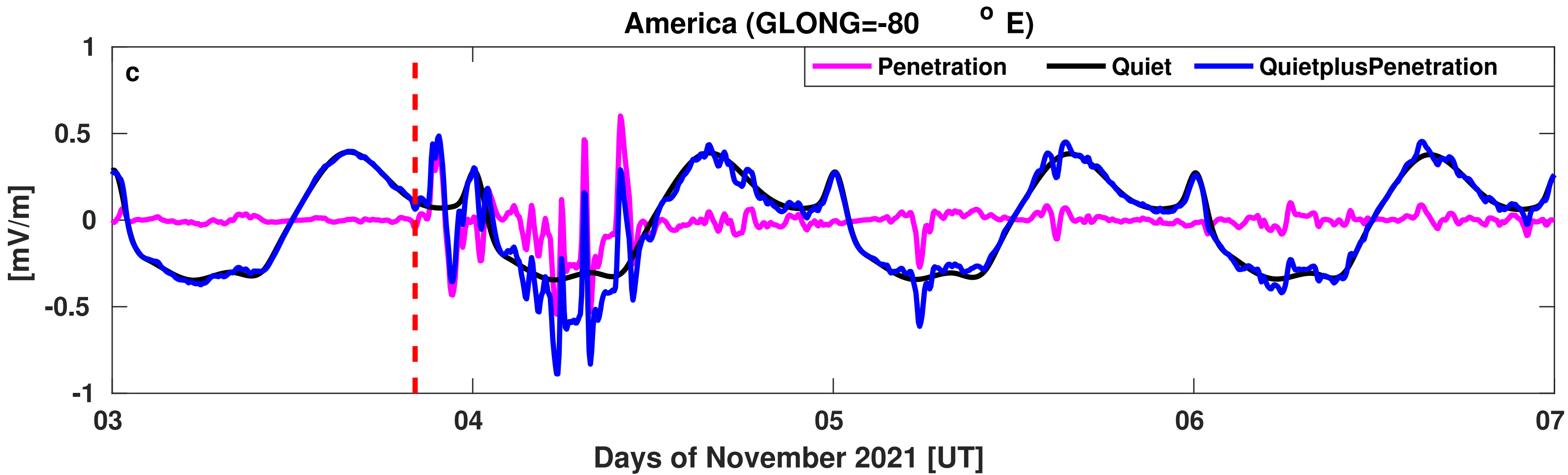
America (GLONG=-80 °E)
c
Penetration
Quiet
QuietplusPenetration
[mV/m]
1
0.5
0
-0.5
-1
03
04
05
06
07
Days of November 2021 [UT]

Figure 5.

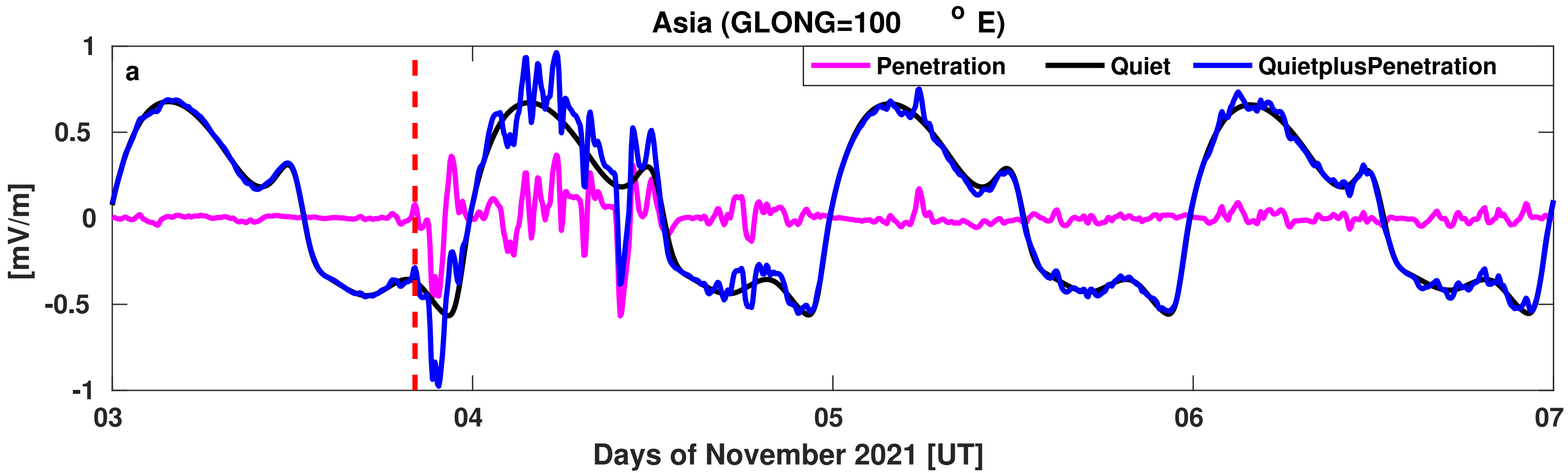

Asia (GLONG=100 ^{o} E)
a
Penetration
Quiet
QuietplusPenetration
1
0.5
0
-0.5
-1
[mV/m]
03
04
05
06
07
Days of November 2021 [UT]

Figure 1.

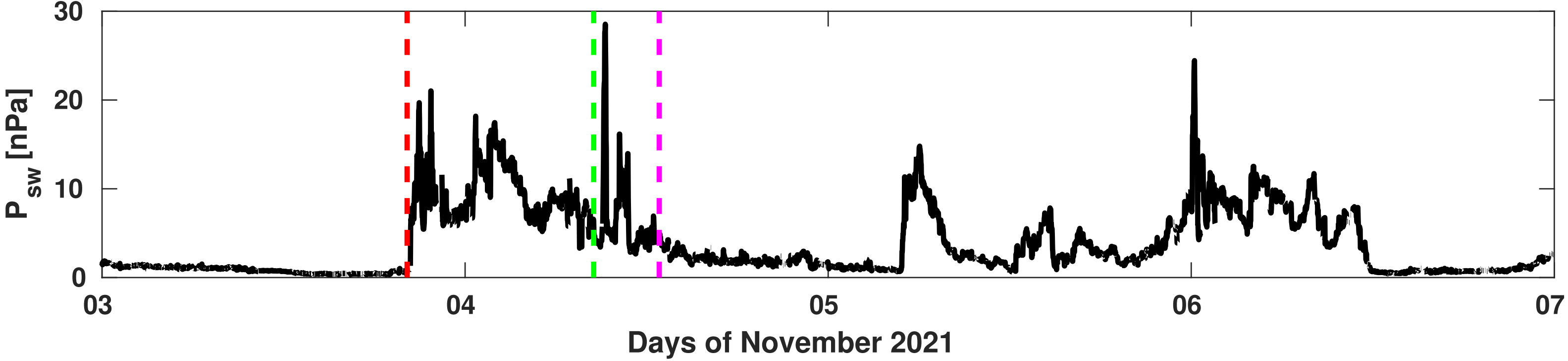

30
20
10
0
P_{sw} [nPa]
03
04
05
06
07
Days of November 2021

Figure 1.

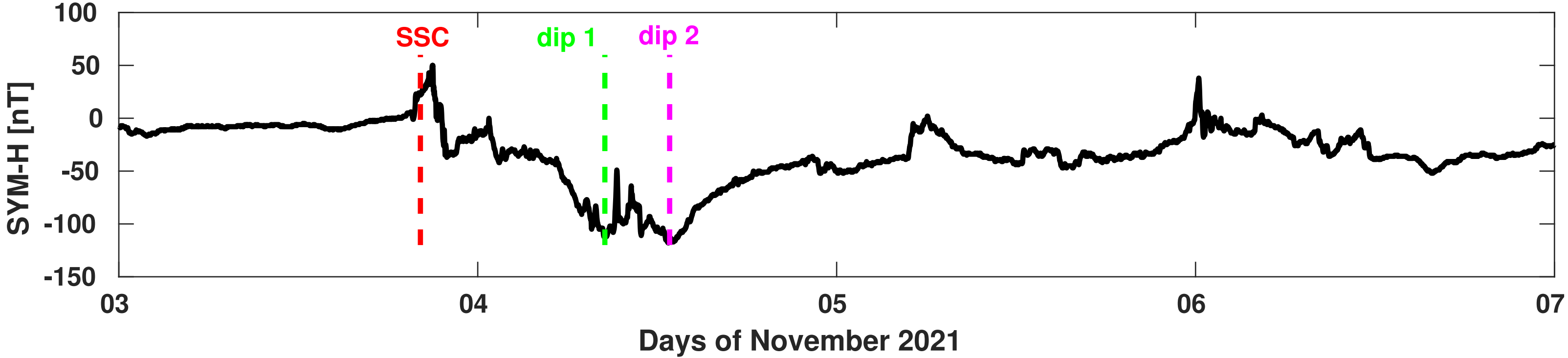

SSC
dip 1
dip 2
SYM-H [nT]
100
50
0
-50
-100
-150
03
04
05
06
07
Days of November 2021

Figure 1.

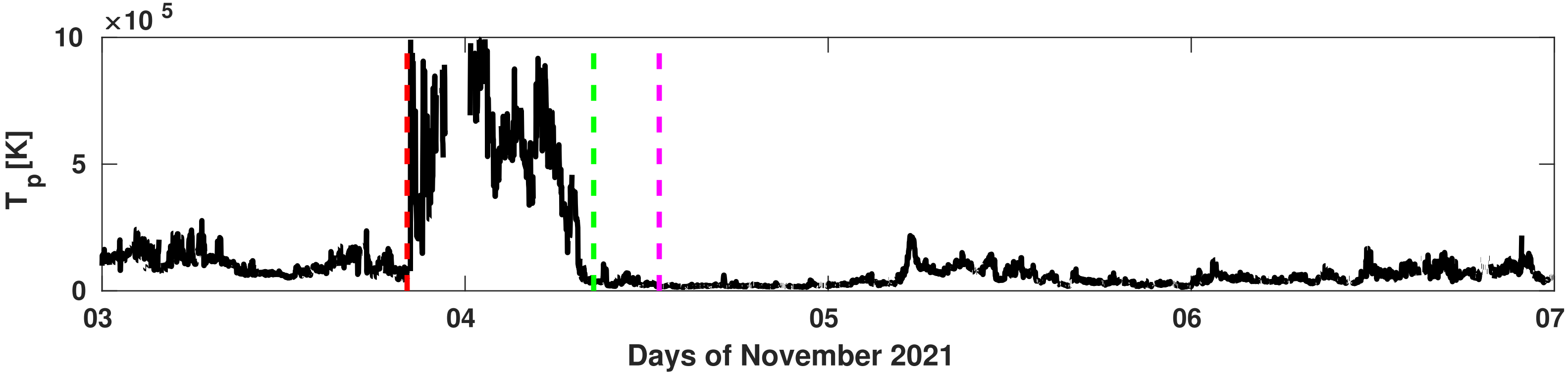

×10 5
10
5
0
T p [K]
03
04
05
06
07
Days of November 2021

Figure 1.

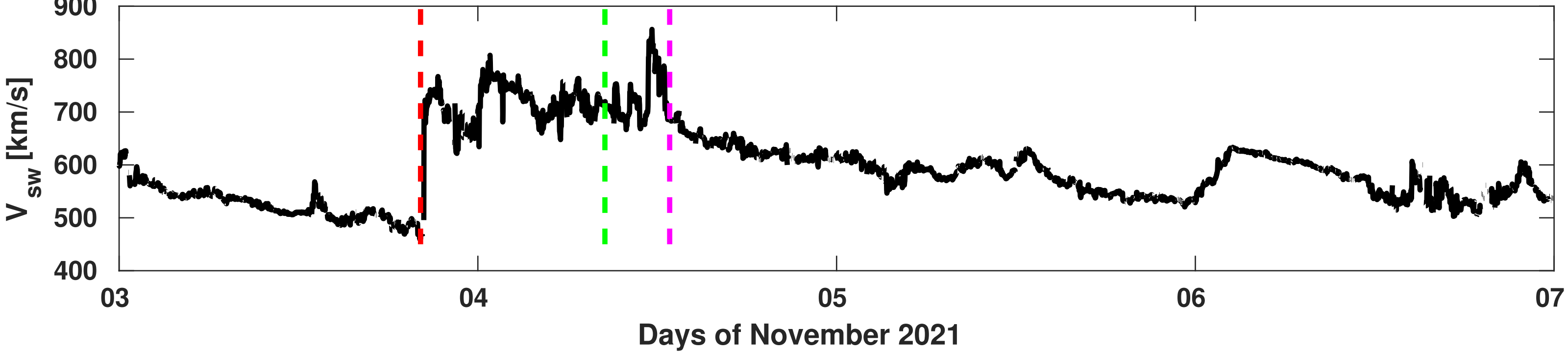
900
800
700
600
500
400
V_sw [km/s]
03
04
05
06
07
Days of November 2021

Figure 1.

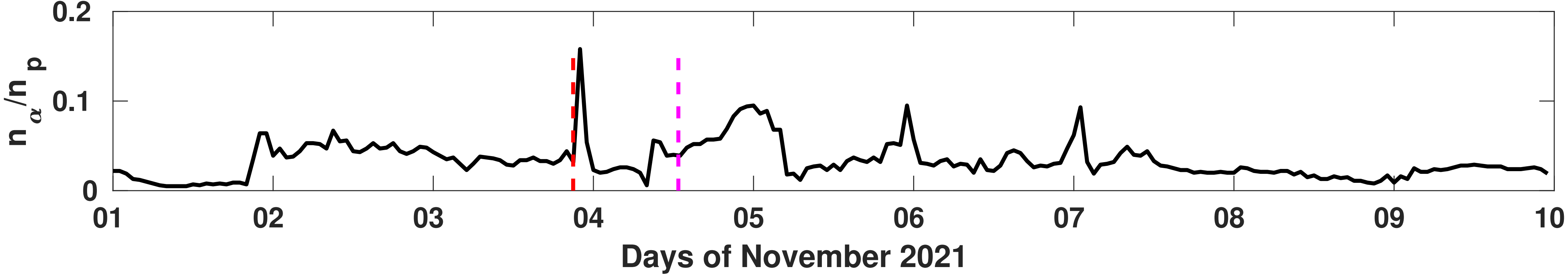

0.2
0.1
0
n_α/n_p
01
02
03
04
05
06
07
08
09
10
Days of November 2021

Figure.

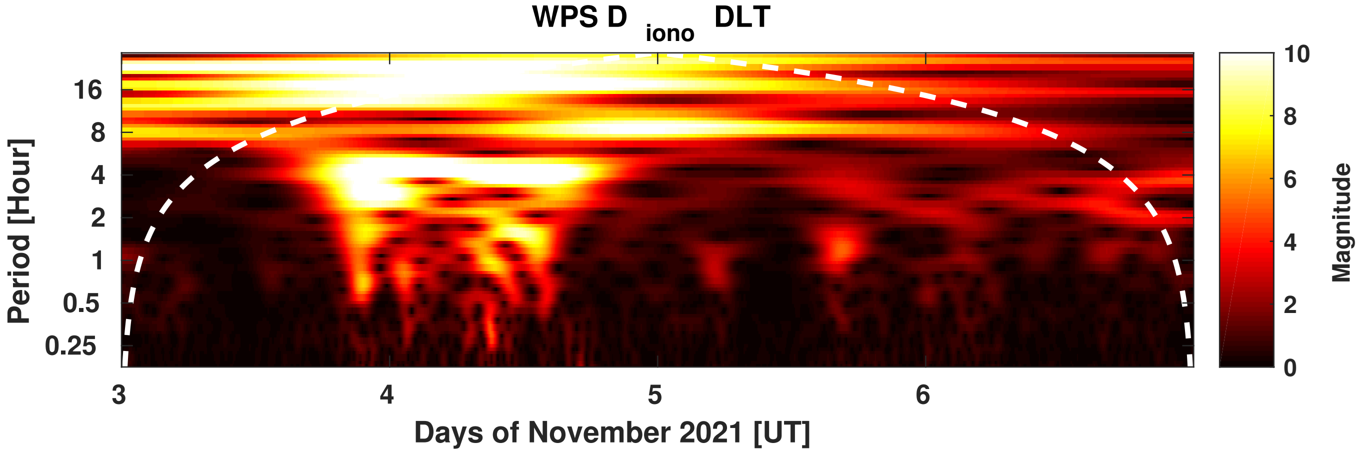

WPS D_{iono} DLT
Period [Hour]
16
8
4
2
1
0.5
0.25
3
4
5
6
Days of November 2021 [UT]
Magnitude
10
8
6
4
2
0

Figure 8.

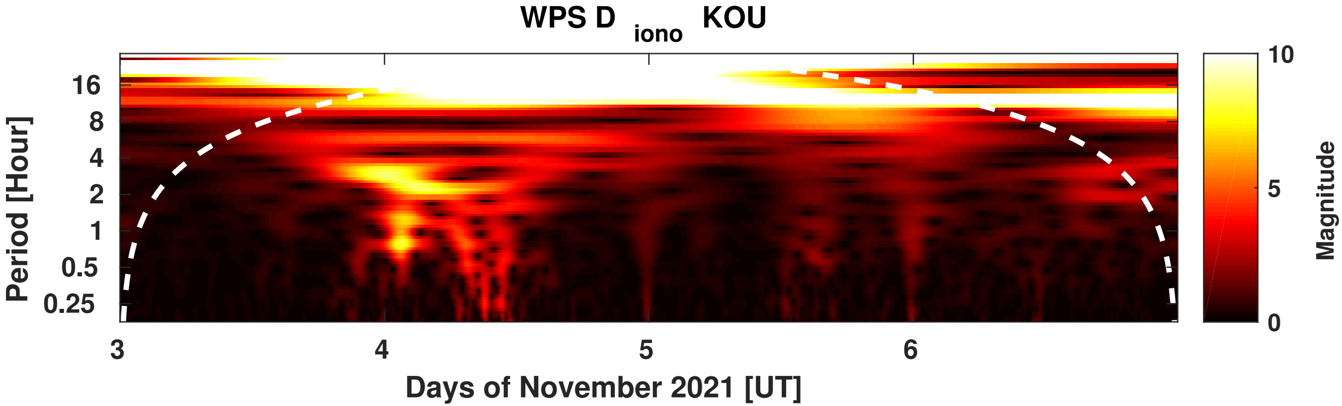

WPS D iono KOU
Period [Hour]
16
8
4
2
1
0.5
0.25
3
4
5
6
Days of November 2021 [UT]
10
5
0
Magnitude

Figure 1.

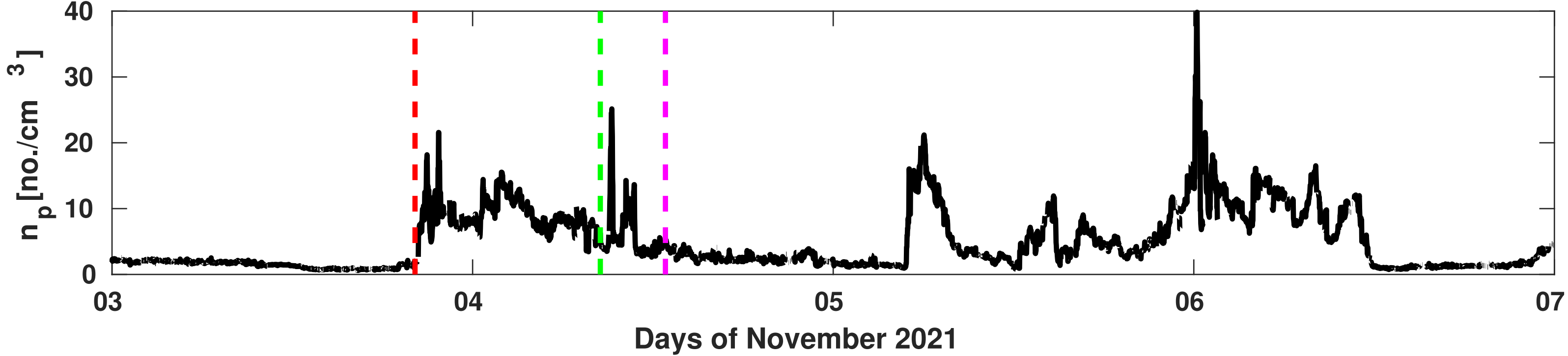

n_p [no./cm^3]
40
30
20
10
0
03
04
05
06
07
Days of November 2021

Figure 4.

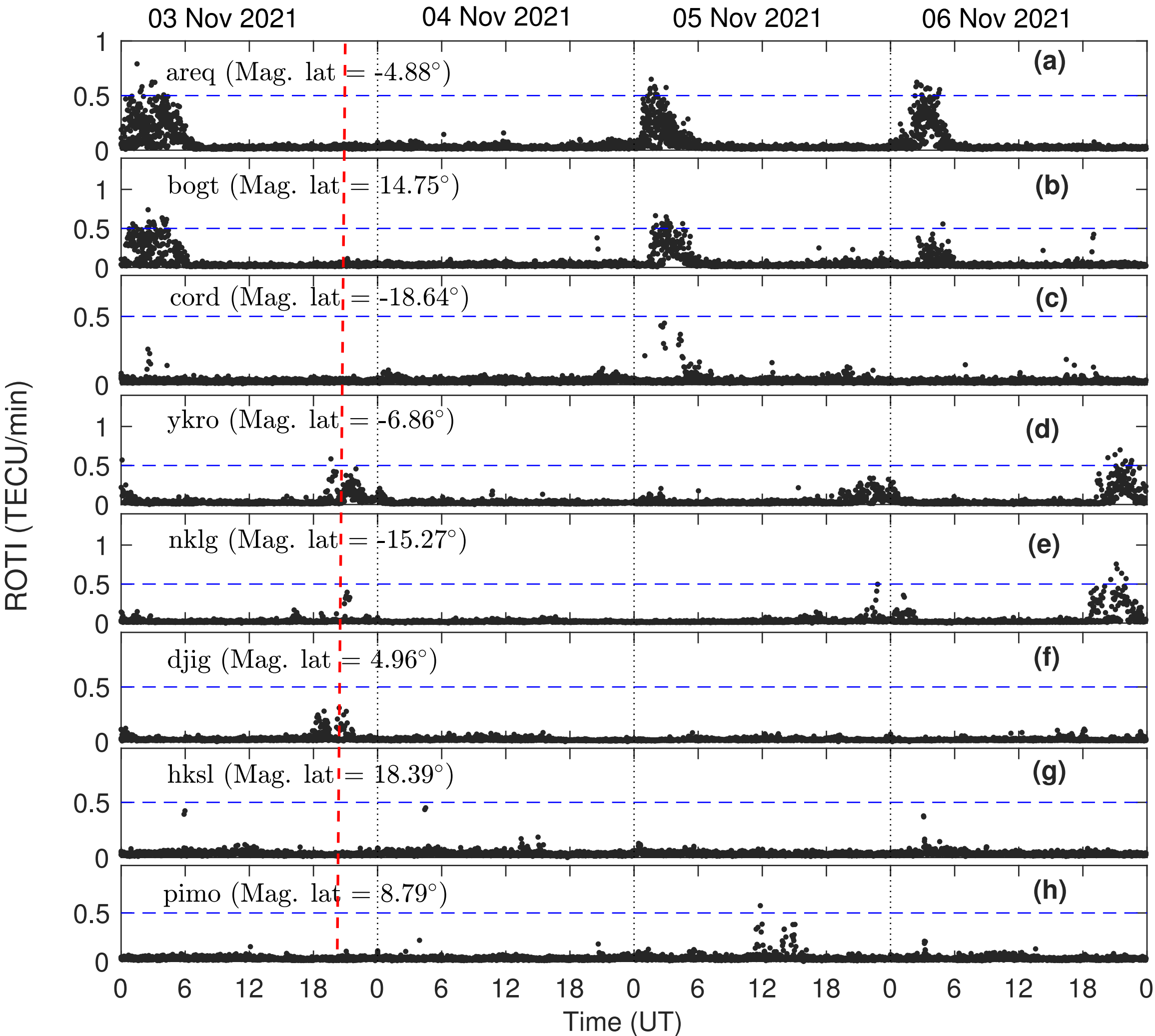
03 Nov 2021
04 Nov 2021
05 Nov 2021
06 Nov 2021
areq (Mag. lat = -4.88°)
(a)
bogt (Mag. lat = 14.75°)
(b)
cord (Mag. lat = -18.64°)
(c)
ykro (Mag. lat = -6.86°)
(d)
nklg (Mag. lat = -15.27°)
(e)
djig (Mag. lat = 4.96°)
(f)
hksl (Mag. lat = 18.39°)
(g)
pimo (Mag. lat = 8.79°)
(h)
ROTI (TECU/min)
Time (UT)

Figure.

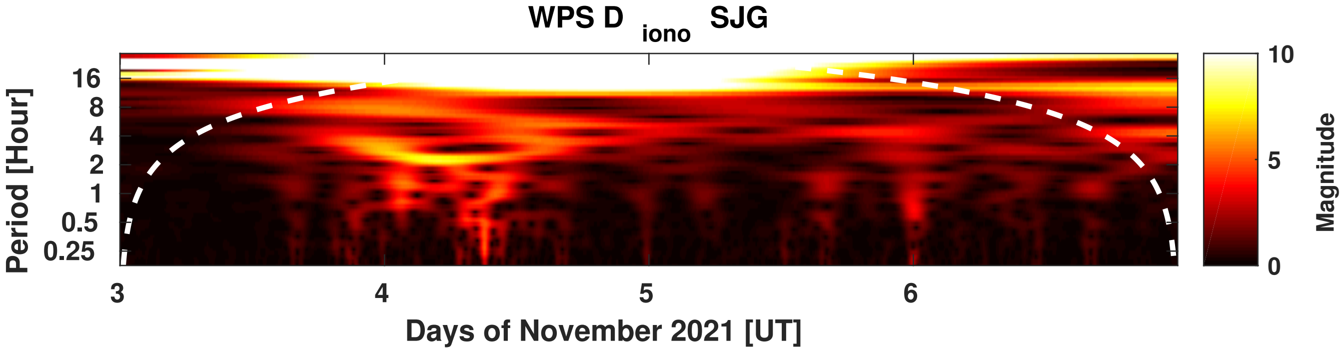
WPS D iono SJG
Period [Hour]
16
8
4
2
1
0.5
0.25
Days of November 2021 [UT]
3
4
5
6
Magnitude
10
5
0

Figure 8.

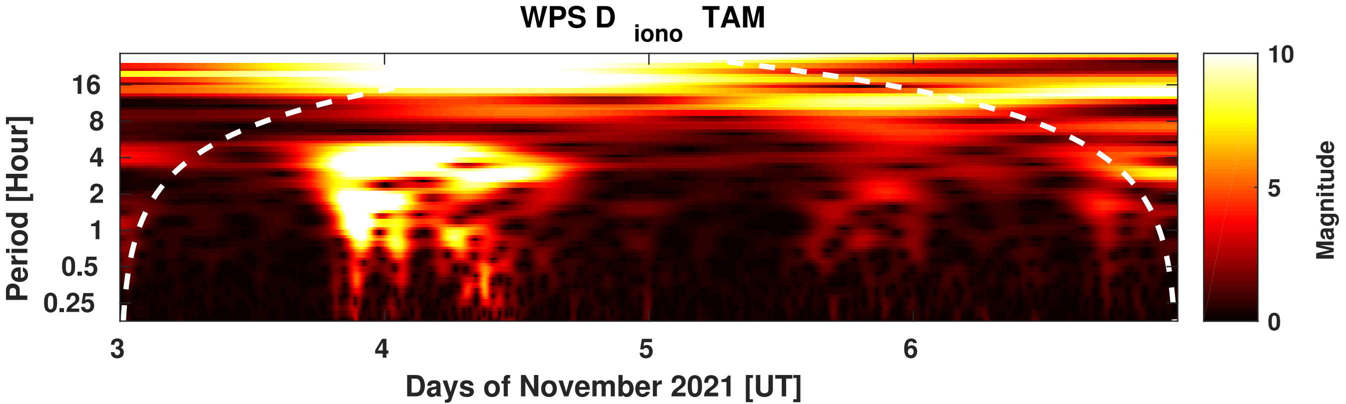

WPS D iono TAM
Period [Hour]
16
8
4
2
1
0.5
0.25
3
4
5
6
Days of November 2021 [UT]
10
5
0
Magnitude

Figure 7.

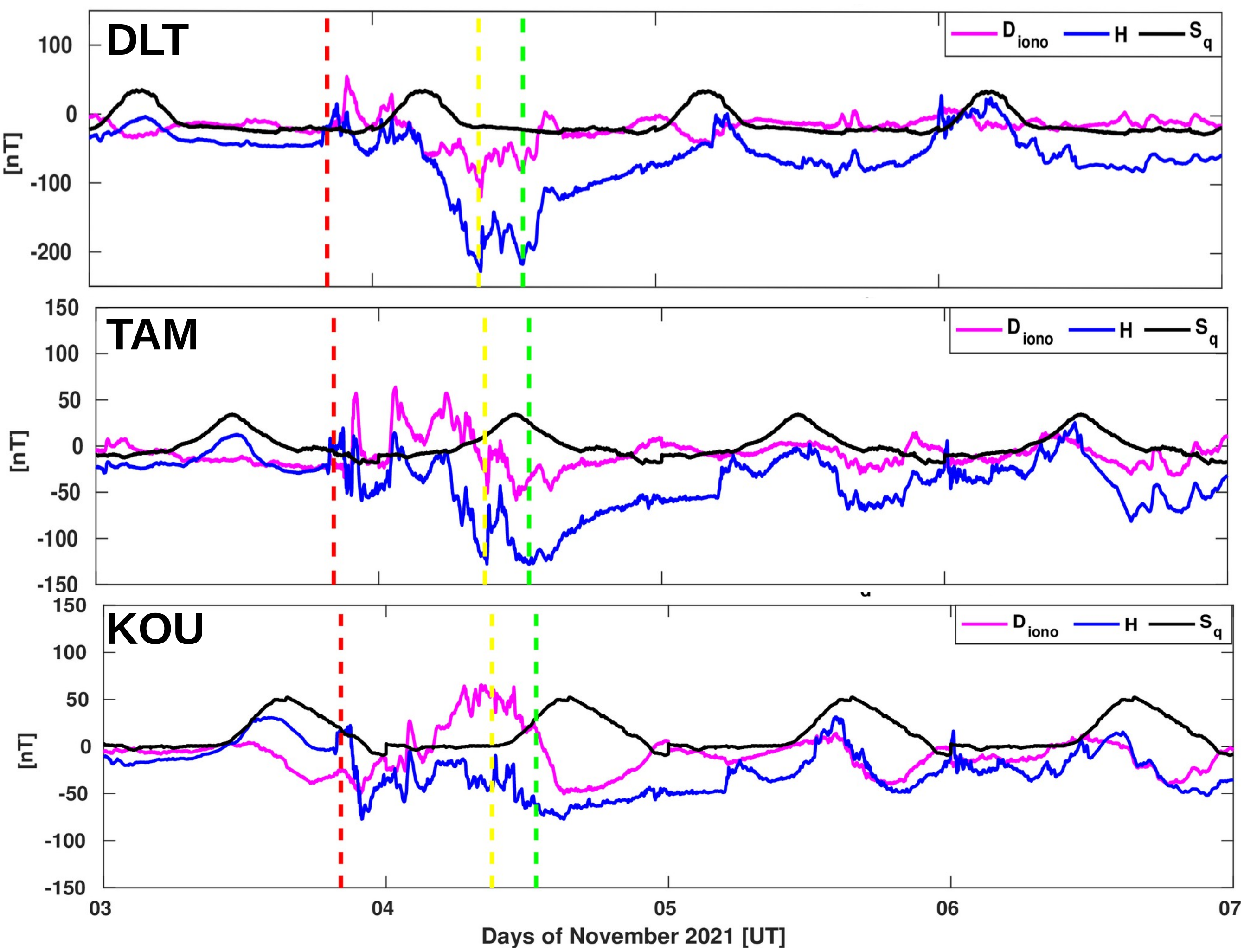

DLT
D iono
H
S q
100
0
-100
-200
[nT]
TAM
150
100
50
0
-50
-100
-150
KOU
03
04
05
06
07
Days of November 2021 [UT]

Figure 2.

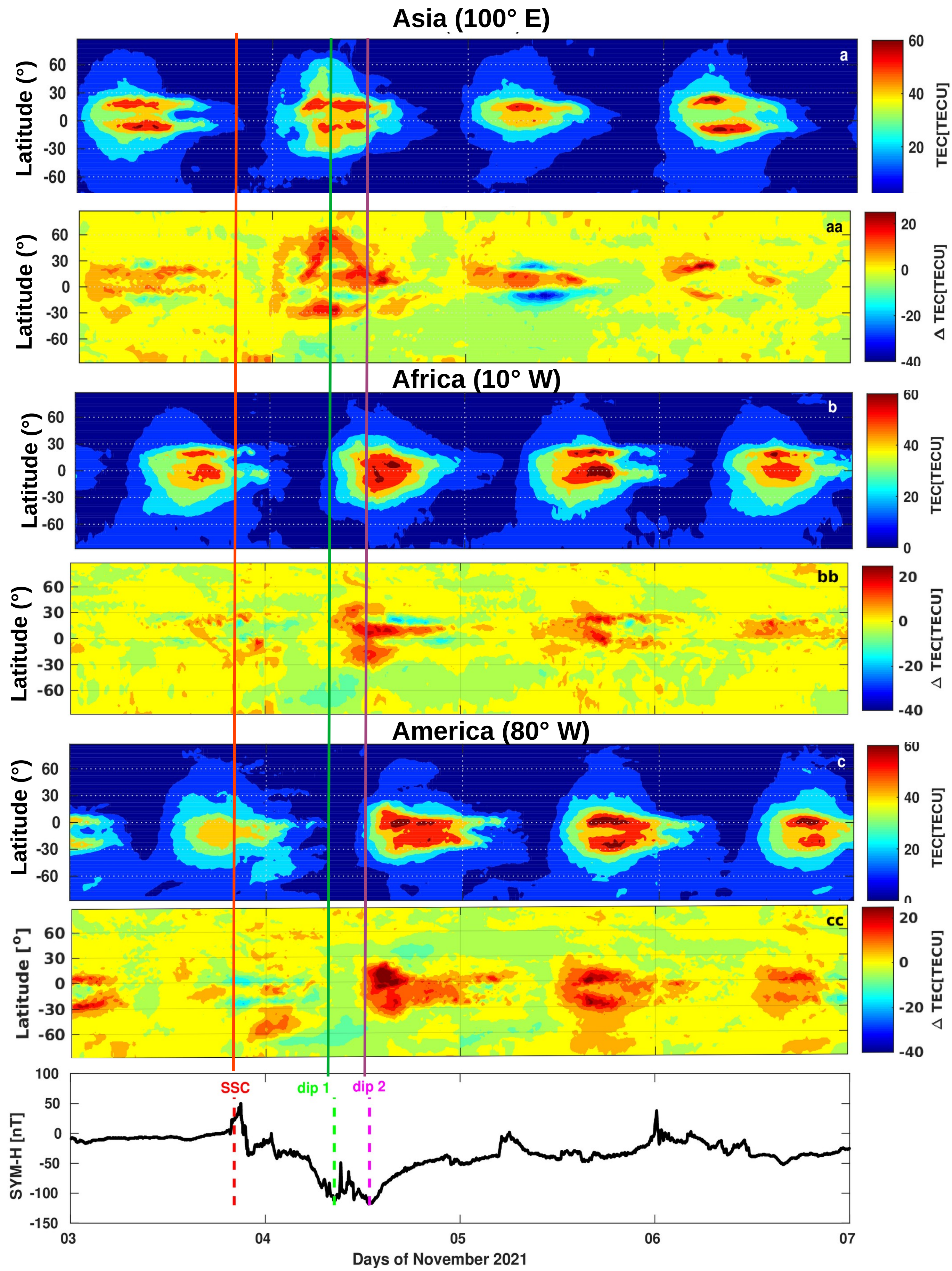

Asia (100° E)
Africa (10° W)
America (80° W)
a
aa
b
bb
c
cc
Latitude (°)
60
30
0
-30
-60
TEC[TECU]
Δ TEC[TECU]
SSC
dip 1
dip 2
SYM-H [nT]
100
50
0
-50
-100
-150
03
04
05
06
07
Days of November 2021

Figure 3.

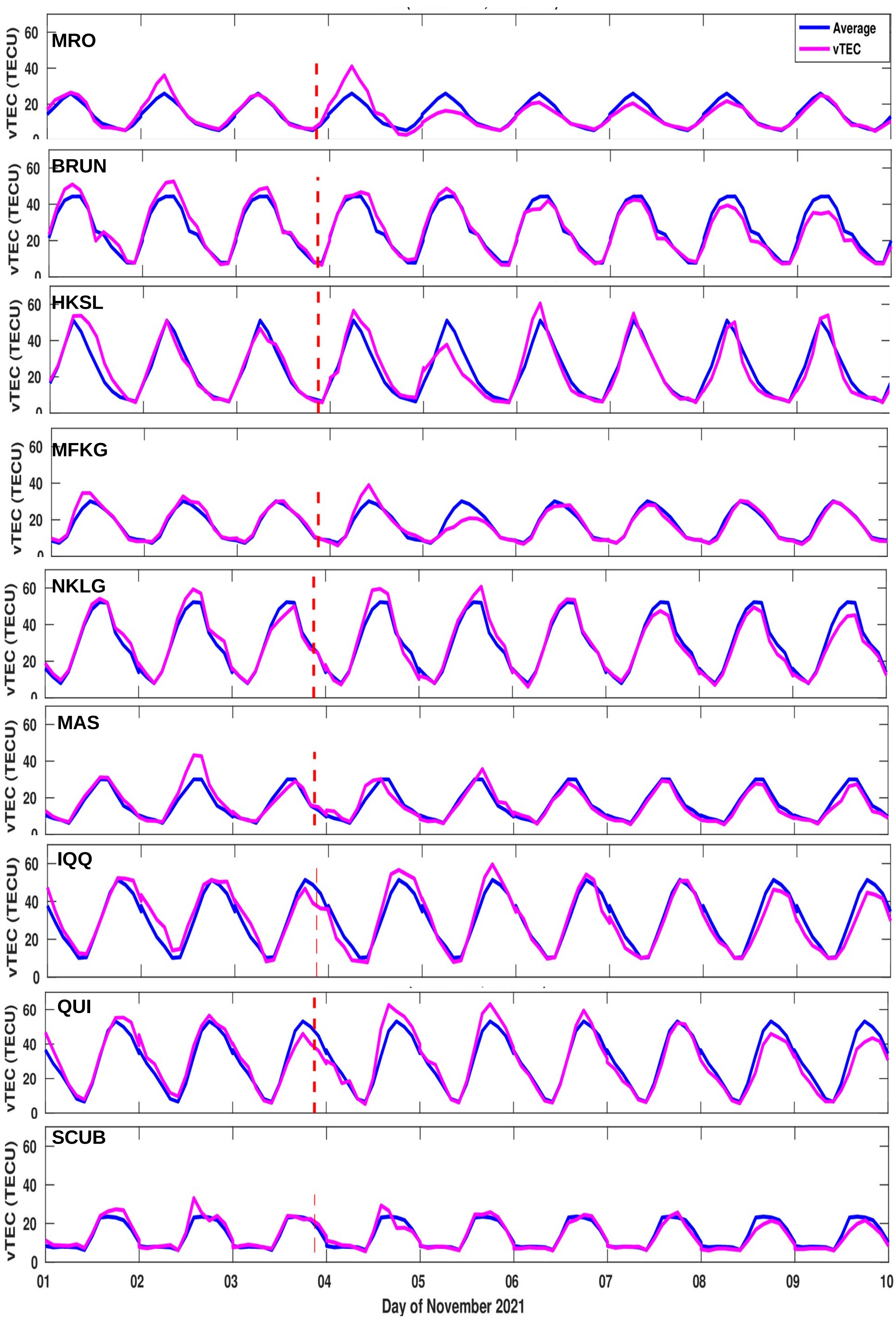

MRO
BRUN
HKSL
MFKG
NKLG
MAS
IQQ
QUI
SCUB
Average
vTEC
vTEC (TECU)
Day of November 2021